NASA Contractor Report 198511

Active Control of Fan Noise: Feasibility Study

Volume 3: Active Fan Noise Cancellation in the NASA Lewis Active Noise Control Fan Facility

Frederic G. Pla and Ziqiang Hu
General Electric Aircraft Engines
Cincinnati, Ohio

Daniel L. Sutliff
Lewis Research Center
Cleveland, Ohio

September 1996

Prepared for
Lewis Research Center
Under Contract NAS3–26617

National Aeronautics and
Space Administration

Active Control of Fan Noise: Feasibility Study
Volume 3: Active Fan Noise Cancellation in the NASA Lewis Active Noise Control Fan Facility

Summary

This report describes the Active Noise Cancellation (ANC) System designed by General Electric and tested in the NASA Lewis Research Center's (LeRC) 48 inch Active Noise Control Fan (ANCF).

The goal of this study is to assess the feasibility of using wall mounted secondary acoustic sources and sensors within the duct of a high bypass turbofan aircraft engine for global active noise cancellation of fan tones. The GE ANC system is based on a modal control approach. A known acoustic mode propagating in the fan duct is canceled using an array of flush-mounted compact sound sources. The canceling modal signal is generated by a modal controller. Inputs to the controller are signals from a shaft encoder and from a microphone array which senses the residual acoustic mode in the duct.

The key results are that the (6,0) was completely eliminated at the 920 Hz design frequency and substantially reduced elsewhere. The total tone power was reduced 6.8 dB (out of a possible 9.8 dB). Farfield reductions of 15 dB (SPL) were obtained. The (4,0) and (4,1) modes were reduced simultaneously yielding a 15 dB PWL decrease. The results indicate that global attenuation of PWL at the target frequency was obtained in the aft quadrant using an ANC actuator and sensor system totally contained within the duct.

The quality of the results depended on precise mode generation. High spillover into spurious modes generated by the ANC actuator array caused less than optimum levels of PWL reduction. The variation in spillover is believed to be due to calibration procedure, but must be confirmed in subsequent tests.

Acknowledgments

The authors would like to acknowledge the support and guidance provided by Laurence Heidelberg of the NASA Lewis Research Center. Special note should be taken of the contributions of Scott Sommerfeldt and Yong-Cheol Park (of Penn State University at the time of this contract) to the development of the control system algorithm, software, and hardware.

Active Control of Fan Noise: Feasibility Study
Volume 3: Active Fan Noise Cancellation in the NASA Lewis Active Noise Control Fan Facility

Table of Contents

Active Control of Fan Noise: Feasibility Study
Volume 3: Active Fan Noise Cancellation in the NASA Lewis Active Noise Control Fan Facility

1. Introduction

This report describes the Active Noise Cancellation (ANC) System designed by General Electric and tested in the NASA Lewis Research Center's (LeRC) 48 inch Active Noise Control Fan (ANCF).

The goal of this study is to assess the feasibility of using wall mounted secondary acoustic sources and sensors within the duct of a high bypass turbofan aircraft engine for active noise cancellation of fan tones.

A schematic of the system designed and tested is shown in Figure 1.1.

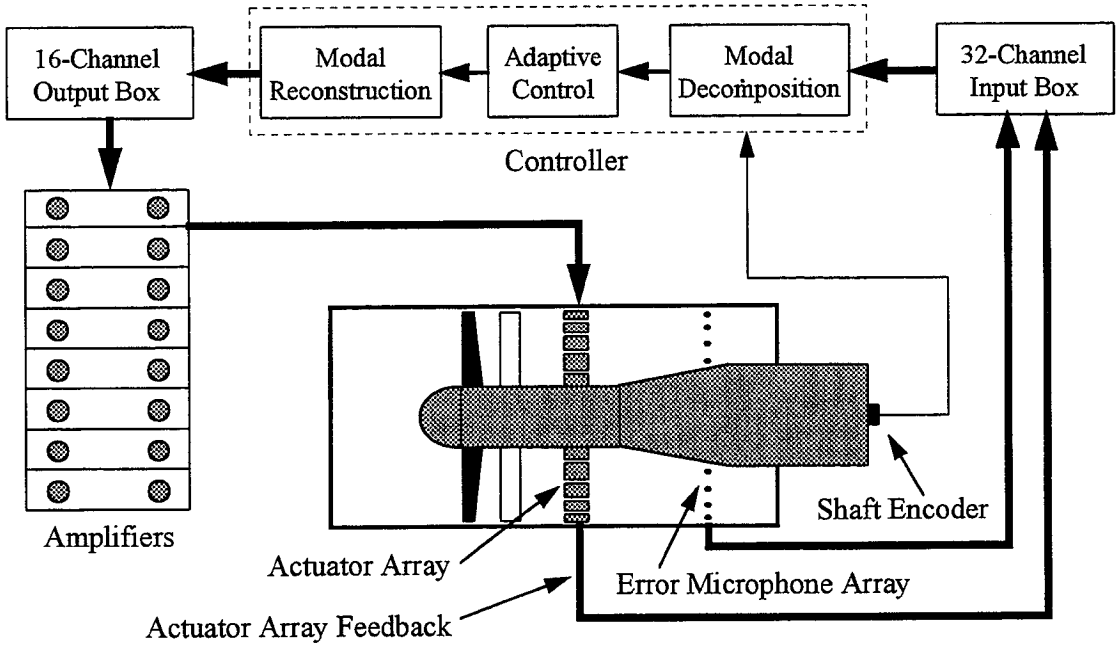

Figure 1.1. GE Active Noise Cancellation system for NASA ANCF facility

The GE ANC system is based on a modal control approach. A known acoustic mode propagating in the fan duct is canceled using an array of flush-mounted compact sound sources. The canceling modal signal is generated by a modal controller. Inputs to the controller are signals from a shaft encoder and from a microphone array which senses the residual acoustic mode in the duct.

The NASA ANCF facility uses a 16-bladed variable-pitch rotor and can be configured with stator vanes to provide specific mode generation and propagation for

Active Noise Control Research. A unique feature on the ANCF is the direct attachment of the rotor centerbody to the rig support column, eliminating the need for struts, which could contaminate acoustic measurements. Additionally, an Inflow Control Device (ICD) allows for static testing. The combination of low tip speed (~400 ft/sec) and the 48 inch diameter produces fan tones of the same frequencies produced by full size advanced engines.

The sections of this report are arranged as follows:

- Actuator array design and implementation
- Controller design and implementation
- System Integration
- Results
- Conclusion and recommendations

2. Actuator Array Design and Implementation

The parameters describing the NASA fan used for this test are given below:

Blade number:	16
Vane number:	26
Exhaust duct diameters:	1.22-m OD, 0.37-m ID
Modes at BPF (m):	All modes cut-off
Modes at 2BPF (m):	
(6,0) cut-on frequency:	651 Hz
(6,1) cut-on frequency:	983 Hz
Maximum RPM:	1886 RPM
Maximum BPF:	503 Hz
Maximum 2BPF:	1006 Hz

A GE Aircraft Engine computer code for acoustic propagation in an annular duct with flow was used to calculate the cutoff frequencies of the various modes inside the 4-foot diameter NASA fan rig.

The fan configuration was chosen such that no modes are cut-on at the Blade Passage Frequency (BPF). The (6,0) mode (m = 6, "0" radial) is cut-on when the fan RPM reaches 64.8% of the maximum speed. The 1053 Hz cut-on frequency for the "first" radial mode (6,1) is outside the maximum RPM range of the fan.

The target RPM for this system was chosen to correspond to a 2BPF tone of 935 Hz. The system was designed to operate with a bandwidth of at least 10%.

The design of the actuator array that generates the canceling sound field consists of several steps:

- *Acoustic array design* - Select the number of array elements and the array solidity. The solidity is defined as the percentage of the duct circumference that is *not* covered by actuator surfaces. (Thus if the total surface of the moving actuators covers 75% of the duct wall circumference, and the inactive (hardwall) segments between the actuators account for the remaining 25%, the solidity is 0.25.) The design procedure includes evaluating the performance of various array configurations to generate a canceling sound field with the desired modal properties.
- *Array element design* - Select array element design parameters such as width, thickness, and material. These parameters can only be determined once the acoustic array design is completed.

2.1. Acoustic Array Design

A simulation tool based on a closed-form analytical simulation has been developed by R. E. Kraft [1] at GE Aircraft Engines to determine the acoustic modes generated by an N-element ring source in a cylindrical duct (see also Volume 6 of the Final Contractor

Report for this program). The simulation was used to design the acoustic array. The solution decomposes the sound field generated by the ring source into its individual modal components. It assumes that the ring source is composed of a number of "piston-like" individual sources. Inputs to the simulation are the number of actuators on the ring source, the mode to be excited, and the source solidity. Results are plotted in terms of the energy in the mode to be excited as well as the spillover energy into undesired higher order modes.

The goal of the acoustic array design is to reach a compromise configuration which minimizes:

- Number and area (solidity) of the actuator elements
- Spillover to uncontrolled higher-order modes
- Energy required by the actuator

Several configurations were evaluated for the m = 6 mode.

Results for 24 source combinations are shown in the table below. The design goal is to determine the minimum number of sources with the highest solidity which is able to generate a high enough acoustic level to cancel the desired mode with minimum spillover into unwanted higher order modes.

Solidity	N = 13	N = 14	N = 15	N = 16	N = 17	N = 18
Modes Generated						
	6, -7	6, -8	6, -9	6, -10	6, -11	6, -12
Port Length (mm)						
1.00E-05	295	274	255	239	225	213
0.25	221	205	192	180	169	160
0.5	147	137	128	120	113	106
0.75	74	68	64	60	56	53
Radius Defect (mm)						
1.00E-05	17.7	15.3	13.3	11.7	10.4	9.3
0.25	10.0	8.6	7.5	6.6	5.8	5.2
0.5	4.4	3.8	3.3	2.9	2.6	2.3
0.75	1.1	1.0	0.8	0.7	0.7	0.6
Energy in m=6 mode (%)						
1.00E-05	24.2	27.1	29.5	31.7	33.5	35.1
0.25	25.4	27.0	28.3	29.4	30.3	31.1
0.5	21.6	22.2	22.6	23.0	23.3	23.6
0.75	12.8	12.9	13.0	13.0	13.1	13.1
(Energy in m=6) / (Energy in next highest mode)						
1.00E-05	1.36	1.78	2.25	2.78	3.36	4.00
0.25	1.17	1.34	1.51	1.68	1.84	2.00
0.5	1.07	1.13	1.19	1.24	1.29	1.33
0.75	1.02	1.03	1.04	1.05	1.06	1.07
Normalized amplitude of M=6-Mode						
1.00E-05	0.69	0.72	0.76	0.78	0.81	0.83
0.25	0.61	0.63	0.64	0.66	0.67	0.68
0.5	0.46	0.46	0.47	0.47	0.48	0.48
0.75	0.25	0.25	0.25	0.25	0.25	0.25

Table 2.1. Array acoustic performance for various array configurations

The variable N represents the number of elements (actuators) in the array.

Results are plotted in Figures 2.1 to 2.4. The energy input into the desired mode and the energy spillover into unwanted higher order modes depends strongly on the number of actuator elements and the ring source solidity. In order to maximize the acoustic energy in the m = 6 mode and minimize the spillover, the number of actuator elements must be maximized and the and the solidity must be minimized. In the range of parameters considered, the solidity is the most important factor.

For a high solidity (higher than 0.50), increasing the number of actuator elements does not increase the array effectiveness significantly. For a low solidity (lower than 0.5), increasing the number of actuators significantly increases the effectiveness of the array by increasing the energy into the m = 6 mode and reducing the spillover.

The actuator configuration chosen for this work had 16 actuators and a solidity equal to 0.25. This represents a good compromise between performance and array complexity and size of each element.

The main array characteristics are given below:

First two modes generated:	6,-10
Circumferential length:	180 mm
Energy in m = 6 mode:	29.4%
Energy in m = 6 mode / Energy in m = -10 mode:	1.68

The performance of a 16-element array is shown in more detail in Figure 2.5 as a function of wall solidity. The energy input by the array into the m = 6 mode is fairly constant for a wall solidity of less than 20% and starts dropping rapidly for a wall solidity higher than 30%. The spillover to the next highest mode (m = -10) increases rapidly as soon as the wall solidity departs from zero. It is very close to one for a solidity higher than 50%.

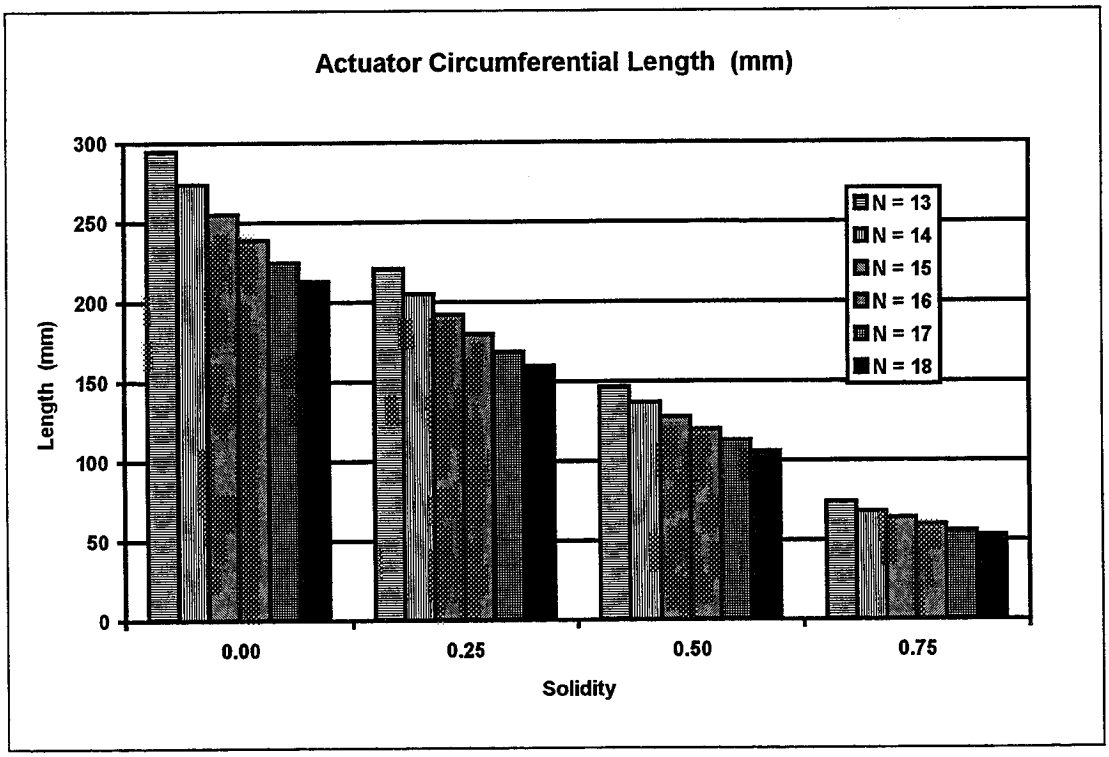

Figure 2.1. Actuator circumferential length versus solidity and number of array elements.

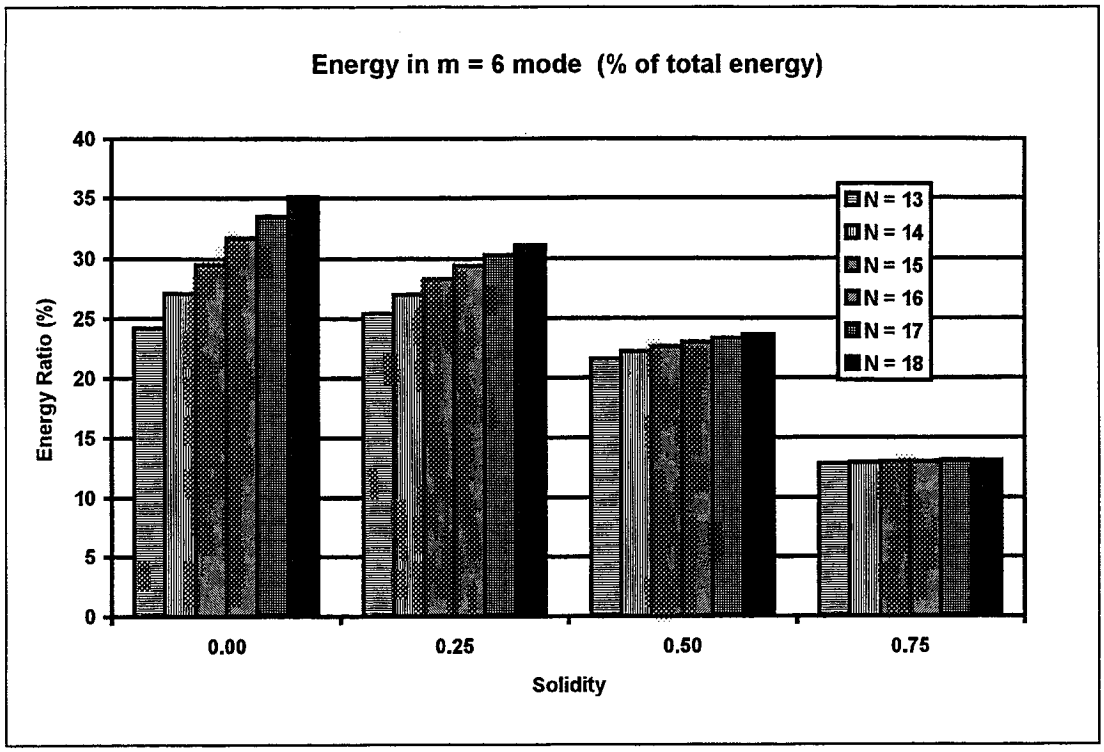

Figure 2.2. Energy in m = 6 mode as a percent of the total energy output

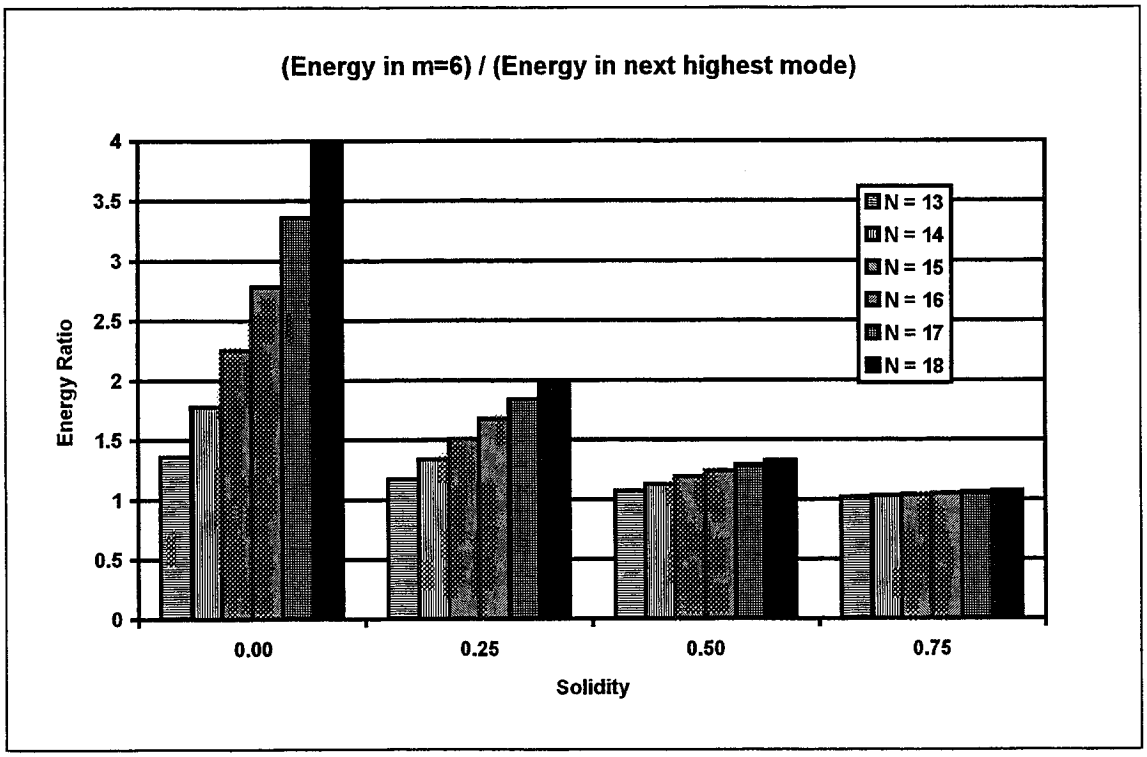

Figure 2.3. Ratio of energy in m = 6 mode to the energy in the next highest mode (see table 2.1)

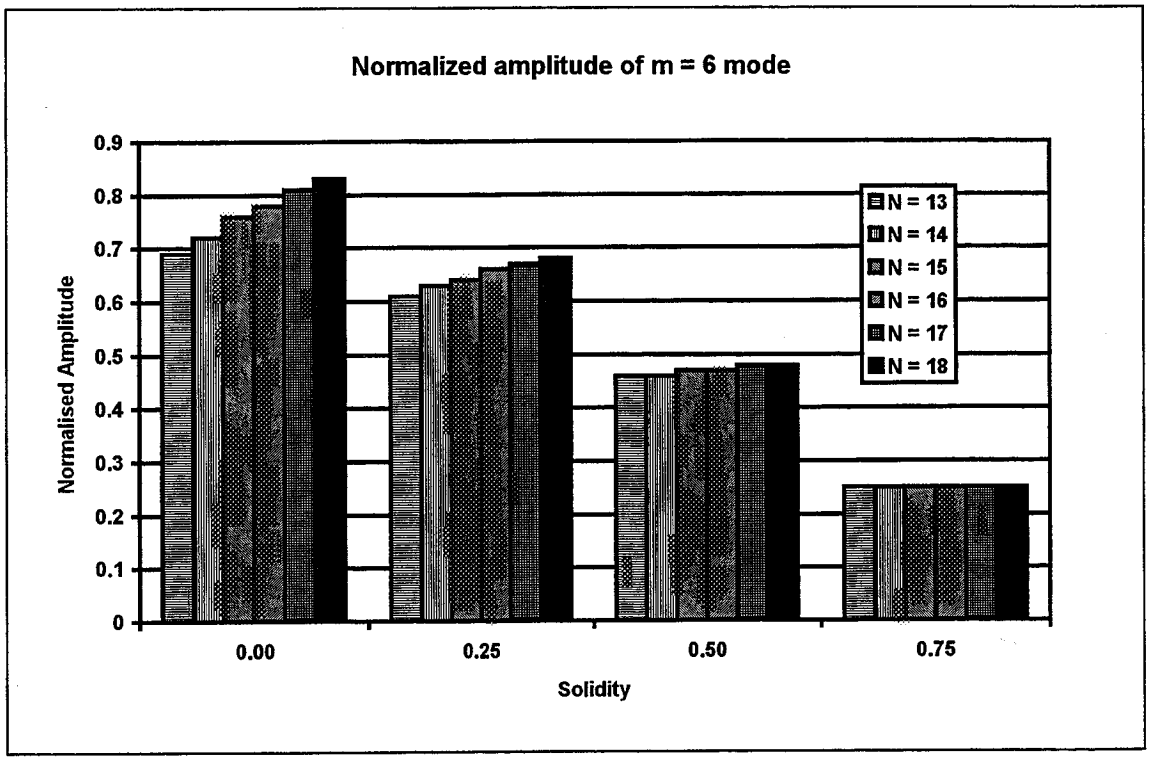

Figure 2.4. Normalized amplitude of m = 6 mode

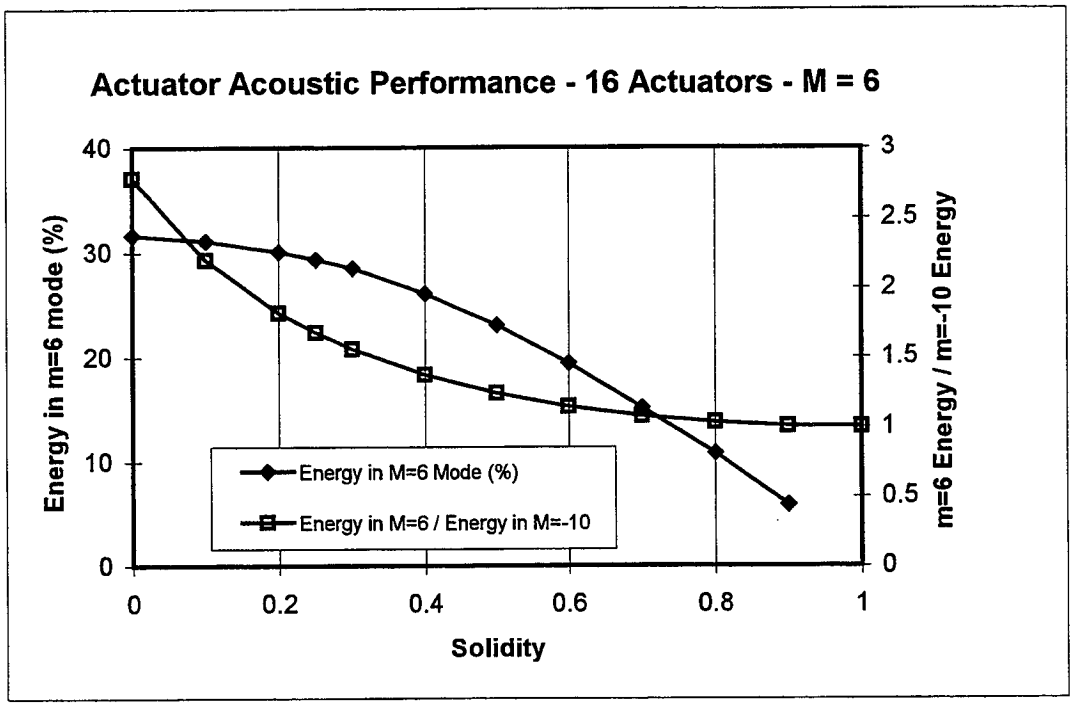

Figure 2.5. (Energy in m = 6 mode) / (Energy in m = -10 mode) - Energy in m = 6 mode as a percent of the total energy output - 16-element array.

2.2. Array Element Design

The results of the array design were used as the basis for a preliminary design of the individual array elements.

Each array element consists of a plate radiator mounted in a frame. The plate radiator is excited by a Piezoceramic (PZT) thin plate bonded to the plate radiator. The plate radiator is designed so that the resonance frequency of its first mode corresponds to the design frequency [2] of 935 Hz .

Analytical models and experimental data were used to estimate the width, thickness, and material of the plate radiator required for a 180 mm length and a first-mode resonance frequency of 935 Hz. Two design iterations were conducted. The final plate design consists of a 2.032-mm thick aluminum plate of dimensions 178 mm by 114 mm.

Mounting and Fine Tuning of Array Element

Several experiments were performed to identify a proper mounting and tuning methods for the plate radiator.

The plate radiators are mounted in a 12.7-mm thick aluminum frame and clamped using a 22-hole bolt pattern torqued to 100 in-lb. A series of test was conducted to investigate variations in resonance frequency for different radiator plates and various assembly processes. Four pairs of plate radiators and PZT actuators were used. Variations in resonance frequency and amplitude were limited to ± 6 Hz and ± 1 dB, respectively. Damping ratio variations were also small.

A 5% variation in the plate first mode resonance frequency, with no significant change in damping ratio and a 20 Hz, 3-dB bandwidth was obtained using a variable clamping force on the frame and the use of 1) 1/8-inch compliant gaskets on each side of the plate 2) 1/16-inch gaskets, and 3) bare frame (no gaskets).

A structural damping material sold by the Sound Coat corporation was also tested to fine tune plate radiators and control their damping. 1-inch by 2-inch and 1/2-inch by 2-inch damping layers were tested. The damping ratios for untreated, and treated (1/2 by 2 and 1 by 2) plates were 1.1%, 1.5% and 2.2%, respectively. The first mode resonance frequency decreased from 907 Hz to 854 Hz to 807 Hz with increasing damping ratio due to the increasing mass loading.

Finally, it was shown that the electric circuit driving the PZT actuator (amplifier and matching circuits) affects the resonance frequency of the assembly by as much as 5% for the design used in this study. This shows that it is feasible to tune the actuator resonance frequency and damping by adjusting the impedance of the matching circuit.

It was concluded that the addition of damping material was the most effective and simple way to tune plate radiators and control their damping for this program. A 1-inch by 2-inch external damping layer was applied to all the plate radiators which raised their damping factor from an average of about 0.5% to approximately 2%.

2.3. Array Element Fabrication

Piezoceramic Actuator

The PZT thin plate actuator was selected after an extensive literature survey, and several consultations with piezoceramic experts from the GE CRD electrical ceramic program, and external experts.

Several types of PZT ceramics were obtained for this study: a "soft-ceramic" as used in previous studies , and two "hard-ceramics" which are expected to provide improved performance at high stress and voltage levels. Only one manufacturer (Morgan Matroc) was found who could provide the hard ceramic material in sheets that were large enough for this test. Because of previous results with soft-ceramic and time constraints, a hard-ceramic PZT only was used for this project. A 50.8-mm square, 0.762-mm thick PZT actuator was used in the final array element configuration.

Bonding Procedure

Several "improved" PZT-to-aluminum bonding agents and processes were identified after consultations with GE CRD and external experts.

Four bonding materials representative of the spectrum of adhesive appropriate for this application were tested: Epotek 377, Araldite AW 106, Tra-Bond F114, and a 2-part CIBA-GEIGY epoxy.

The Epotek 377 has the highest lap shear strength of all the epoxy surveyed. It also has a very high curing temperature (150 deg C). The other bonding materials have lower lap shear strength but also lower curing temperatures.

A test fixture and test radiator plates were designed and fabricated to allow repeatable testing of the various bonding agents and processes. The test fixture was also used to perform PZT pre-stressing tests. The fixture was mounted inside an environmental chamber including a vacuum bell jar, vacuum pump, hot plate, and heat transfer plate for the bell jar.

Bonding techniques were developed using 10-mil transparent glass plates instead of the PZT thin sheets. This allowed the quality of the bonding process to be evaluated and minimized testing cost.

Some of the bonding processes investigated include:

- Plate preparation
- Low temperature and high temperature degassing
- Even 1.6-mil wet bond layer application using wire-wound rods
- High-temperature curing procedures
- Effect of thermal coefficient mismatch on curing procedure and actuator pre-stressing.

The effect of the mismatch between the thermal expansion coefficients of the aluminum plate, bonding layer, and PZT actuator was found to be very important. In cases where the actuator was bonded to the plate at room temperature and then cured at high temperature, the thermal coefficient mismatch was high enough that high stress levels

resulted in cracks in the PZT actuator. By changing the curing process, the mismatch in thermal expansion coefficients was used to pre-stress the PZT ceramic and increase its dynamic range.

The final bonding process used for this project was established after much experimentation. The electrodeless mounting with two kinds of epoxy is described below:

The epoxies (CIBA-GEIGY 2-part conductive epoxy and Epotek EP110 conductive epoxy) are initially degassed for 1 1/2 hours with venting performed at 15-minute intervals. A 2-mil layer of non-conductive epoxy is applied to the PZT using a 2-mil tape. The use of a tape seems to result in less air pockets in the bond layer than the use of a wire wound rod. Conductive epoxy is then applied to specific "spot" locations on the PZT element to ensure adequate electrical contact between the diaphragm and the bottom PZT electrode. Since the conductive epoxy is chemically compatible with the structural epoxy but has a much lower lap shear strength, it is only used in "spot applications" at locations where stresses are the lowest: at the center of each side of the plate. This forms an electrodeless actuator which minimizes residual stresses and increases the actuator dynamic range. Next, the PZT element is centered on the preheated aluminum plate radiator. Pressure is applied to the actuator to remove bubbles in the bonding layer. Finally, the plate is cured at 150 deg. F for 1.5 hour with a 1-psi pressure applied to the element.

2.4. Array Element Feedback Sensor

A feedback sensor was designed and implemented to provide real-time feedback of the amplitude and phase of the volume velocity of each array element. Feedback is obtained using a transducer mounted inside back chamber of each array element.

The sound pressure in the back chamber of the existing plate radiator was estimated to be about 145 dB when the array generates a 120-dB, m = 6 mode in a 4-foot diameter duct. Since this sound pressure level is too high for typical electret microphones, alternative low-cost pressure sensor designs were investigated. The final choice was a 2-inch diameter low-cost voice-coil audio speaker. The speaker can sense a sound pressure level up to 150 dB with less than 1% harmonic distortion. The amplitude and phase frequency response are within 5 dB and 3 degrees respectively in the frequency range of interest (700 Hz to 1000 Hz).

Figure 2.6 shows a diagram of the final array element configuration.

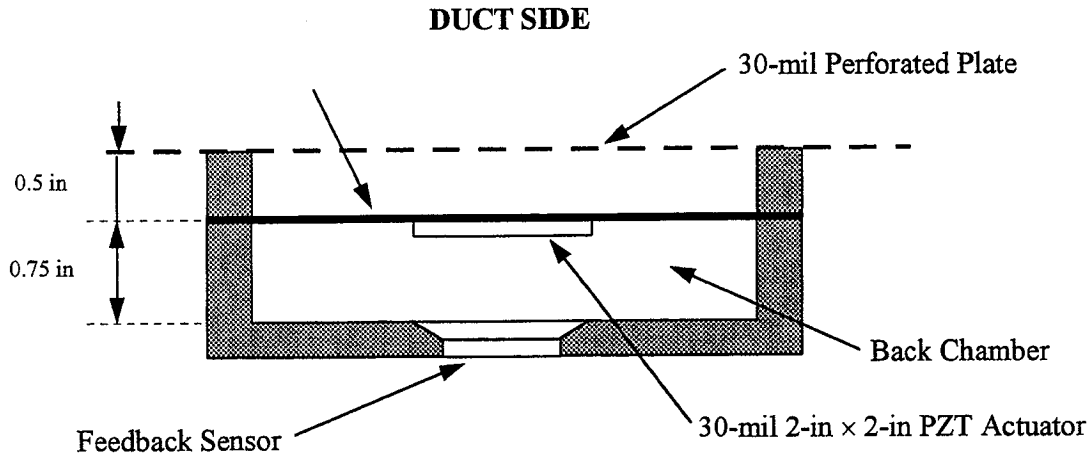

Figure 2.6. Array element schematic

2.5. Array Element Testing

Long term reliability testing for the plate radiator/PZT actuator combination was conducted. The plate radiator was run successfully for 340 hours at a sound pressure level of 130 dB (PZT actuator driven at 80 Vrms), and for 170 hours at 134 dB measured 50.8 mm away from the center of the diaphragm.

3. Controller Design and Implementation

This section describes the design and implementation of the ANC controller for the NASA fan.

3.1. Review of Control Approaches

Several control approaches were reviewed including time-domain LMS, frequency-domain, and modal control approaches. For each approach, benefits, limitations, cost, flexibility, performance, and vendor availability were evaluated so that the best approach could be selected by GE and NASA.

Prior to the start of this Contract, GEAE had provided IR&D funding to Virginia Polytechnic Institute and State University to develop and evaluate frequency domain and time domain control system algorithms for application to turbofan ANC systems. The results of these studies were an integral part of the evaluation of the various control system strategies that is described below.

3.1.1. Time-domain control strategy

The following approaches were reviewed

- Filtered-X LMS with off-line system identification
- Filtered-X LMS with on-line system identification
- Block time-domain LMS
- Direct error-gradient estimation LMS algorithm

Time-domain and frequency-domain control schemes usually attempt to minimize noise at a number of locations using a number of canceling sources. One drawback of these methods is that noise minimization is performed at the error sensor locations. In the aircraft engine noise case, the error sensor locations (most probably inside the fan duct) and the locations where noise must be minimized (far-field) are different. Experience has shown that performance is usually poor with such an arrangement.

Time-domain algorithms based on the filtered-X LMS approach are commonly used. They are simple, fast, flexible, and very effective in situations where noise reduction must be achieved at several localized points. However, since no error sensor can be placed in the far-field of an aircraft engine, the effectiveness of this approach is questionable. In addition, the complexity of these methods increases rapidly with the number of input and output channels making it difficult to use when large numbers of actuators and sensors are required.

Another drawback of the time-domain approach is its inability to discriminate between various acoustic modes or frequency components. As a result, time-domain algorithms offer little control over how and where noise is minimized. Additional pre- and

post- processing can be incorporated to the algorithms to increase their frequency and modal selectivity, effectively turning them into frequency-domain or modal algorithms.

Time-domain filtered-X algorithms with off-line or on-line system identification are the most commonly used active noise control algorithms. The block time-domain LMS algorithm is a variation of the standard time-domain LMS method which uses an averaging scheme allowing the controller filter coefficients to be updated only at regular intervals, thus reducing the computational load. The direct error-gradient estimation LMS algorithm does not require system identification because it measures the "true error" gradient of the system. However, it is computationally more intensive than the standard LMS algorithm.

3.1.2. Frequency-domain control strategy

The following approaches were reviewed

- Circular-convolution filtered-X LMS with on- or off-line system identification
- Linear-convolution filtered-X LMS with on- or off-line system identification
- Sliding-DFT complex LMS

Frequency-domain algorithms were the first algorithms used in active noise control. They are typically more complex than time-domain algorithms since the signals must be transformed into the frequency domain, processed, and then transformed back into the time domain.

Since the frequency-domain transformation is orthogonal, each individual frequency component can be canceled individually, thus allowing for a frequency-selective control, and a fairly uniform convergence rate. However, frequency-domain algorithms suffer from most of the same problems as time-domain algorithms do: no modal selectivity, noise cancellation at the error sensors and not necessarily in the far field, and a complexity which increases rapidly with the number of input and output channels.

The frequency-domain approach can be implemented using a filtered-X LMS algorithm similar to the time-domain algorithm with on-line or off-line system identification. Either a circular or linear convolution approach can be used. The circular convolution is less complex than the linear convolution although its performance might not be as good for closely spaced frequencies. The sliding-FFT algorithm is a hybrid approach similar to the time-domain LMS except for the fact that the input signal is pre-filtered by a bank of band-pass filters using a DFT algorithm. This frequency transformation orthogonalizes the signal which allows independent control of the individual frequency components and improves convergence characteristics.

The computational complexity of the various time- and frequency-domain algorithms depends on the "filter size". When a large filter size is required such as when many different frequencies must be canceled, frequency-domain algorithms are usually faster. When a small filter size is required such as in the case of fan noise cancellation where only a few frequencies must be canceled, time-domain algorithms are typically faster.

It should be pointed out that there is an infinite number of variations of these algorithms that can be used to cancel fan noise, each with its respective set of advantages and drawbacks. The choice of algorithm depends on the level of level of performance required, and the hardware and processing power available.

3.1.3. Modal Control Strategy

A modal control strategy is being developed at GE CRD for the active control of fan noise. This approach has the potential to be much simpler than the time- or frequency-domain approaches. In addition, it allows the individual control of each acoustic mode propagating in the fan duct which in turn allows a much better control over the far-field noise radiation than the standard time- or frequency-domain approaches.

The basic principle is as follows: The composite primary and canceling sound field is sensed by an array of error sensors located in the engine duct. A modal decomposition is performed using a spatial Fourier transform to extract the amplitude and phase of each mode to be canceled. This signal is then used to adjust the amplitude and phase of each "canceling mode" using an algorithm such as the LMS algorithm. An inverse spatial Fourier transform is then performed on the "canceling mode" signal to generate the canceling signals for each individual canceling source.

One of the advantage of the modal approach is its simplicity and its ability to control modes individually. This approach blends the effectiveness of existing control algorithms with the physical understanding of duct acoustics to provide an efficient and simple control scheme. The controller size is independent of the number of error sensors and canceling sources since it is reduced to a set of independent single-input, single-output controllers - one for each mode to be canceled.

This approach considerably reduces the complexity of the controller compared to conventional time-domain or frequency domain control schemes. Increased resolution can be achieved by simply increasing the number of sensors and actuators. As with the time- and frequency-domain approaches, one critical element is the ability of the sensors and actuators to maintain known phase and amplitude characteristics. This requires on-line or off-line actuator and sensor system identification to be performed depending on their amplitude and phase stability.

3.2. Modal Control Algorithm

The controller design was performed assuming the following design variables and assumptions"

- The fan duct is annular
- The primary noise source is tonal and due to rotor/stator interactions
- One mode at one frequency must be canceled
- A 16-source circumferential array of wall-mounted plate radiators is used as the secondary canceling source.

- Error sensing is performed with a circumferential microphone array
- A tachometer signal is available as a frequency reference signal
- Primary (fan) and secondary (canceling array) sources do not affect each other
- Only one circumferential mode is cut-on in the frequency range of interest.
- Sound propagation in the duct is linear.
- Little sound reflection at the duct opening

3.2.1. Modal Control Concept

The modal control approach is described in Figure 3.1.

The fan noise is generated by interactions between rotor blades and stator vanes. The primary noise is tonal and propagates upstream and downstream of the fan duct in the form of circumferential and radial modes. For the purpose of this work, only circumferential modes are considered. For a given fan rotational speed $\Omega(s)$ (s is the Laplace variable) and duct geometry, the modal composition of the sound field is well known.

This information is used by the controller to generate a canceling sound field using an array of secondary sources. The total noise $E(\theta, s)$ (θ is the circumferential angle) in the mode of interest (mode m) at the microphone array is equal to the sum of the primary fan noise $D(\theta, s)$ and the secondary canceling noise $Y(\theta,s)$ for that mode. The goal of the control system is to adjust the amplitude and phase of the mode generated by the secondary sources in order to minimize the amplitude of mode m in the duct.

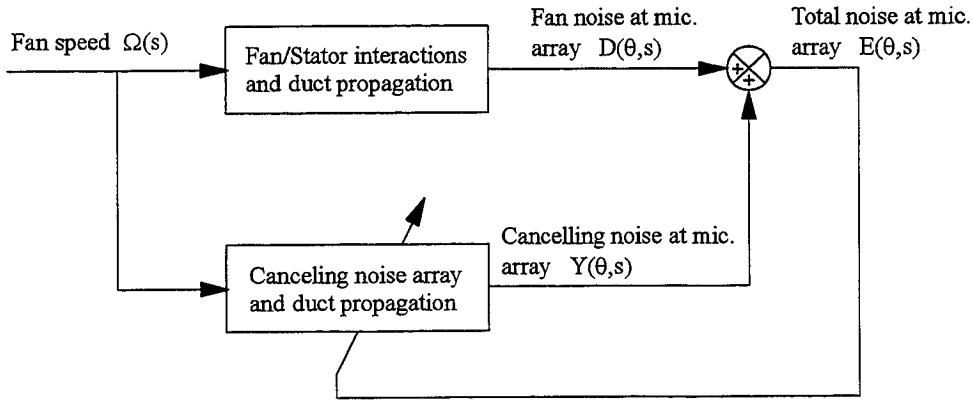

Figure 3.1. Modal control approach - Concept

3.2.2. Modal Control Algorithm

The primary and secondary acoustic fields can be represented as shown in Figure 3.2.

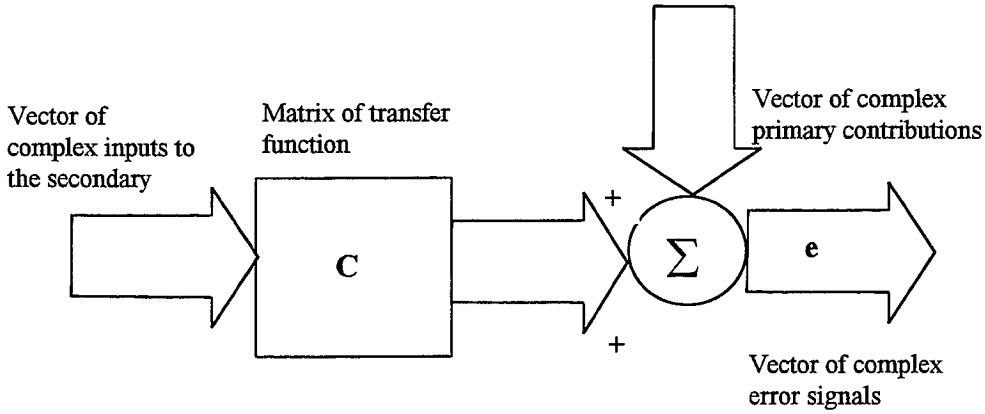

Figure 3.2. Multi-channel control system response at steady state - Block diagram.

The vector of complex response at each microphone can be expressed by using the matrix representation given by

$$\mathbf{e} = \mathbf{d} + \mathbf{C}\mathbf{y} \tag{3.1}$$

where the complex vectors **e, d** and **y** are defined as error signals, microphone inputs with primary source operating alone and inputs to the secondary sources, respectively. The complex matrix **C** represents the transfer functions from the input to the secondary sources to the output of the microphone array system.

Generalized cost function and minimum noise solution

A cost function can be defined as the sum of the squared moduli of the outputs from all the error microphones:

$$J = \sum_{l=1}^{N} \left| e_l \right|^2 = \mathbf{e}^{\mathrm{H}}\mathbf{e} \tag{3.2}$$

By minimizing the cost function J with respect to **y**, we obtain:

$$\mathbf{y}_o = -(\mathbf{C}^{\mathrm{H}}\mathbf{C})^{-1}\mathbf{C}^{\mathrm{H}}\mathbf{d}. \tag{3.3}$$

Although the exact least squares solution discussed above is available, there are a number of practical problems associated with its direct computation in a practical control system. Iterative algorithms have been found to be very effective in solving this problem. The best known algorithm of this type is the Gauss-Newton method. It can be written as:

$$\mathbf{y}(k) = \mathbf{y}(k-1) - \mu[\mathbf{C}^{\mathrm{H}}\mathbf{C}]^{-1}\mathbf{C}^{\mathrm{H}}\mathbf{e}(k-1). \tag{3.4}$$

The variables are defined as follows: $\mathbf{e}(k)$ is the vector of error signals at the k^{th} iteration; $\mathbf{y}(k)$ and $\mathbf{e}(k)$ are the vector of signals to the secondary sources and the error signal vector, respectively at the k^{th} iteration. μ is the step size. In the case where the number of secondary sources is the same as the number of error sensors, the matrix $\mathbf{C}$ is square and Newton's method reduces to

$$\mathbf{y}(k) = \mathbf{y}(k-1) - \mu\mathbf{C}^{-1}\mathbf{e}(k-1) \tag{3.5}$$

Newton's method provides a very direct convergence to the exact least squares solution. However, if the problem is ill-conditioned the exact least squares solution can, in some cases, involve excessively large signals driving the secondary sources. The problem can be alleviated by introducing an "effort" term and a "rate" term in the cost function as follows:

$$J_d(k) = [\mathbf{e}(k) - \mathbf{e}_{des}]^H[\mathbf{e}(k) - \mathbf{e}_{des}] + \lambda_1\mathbf{y}^H(k)\mathbf{y}(k) + \lambda_2\Delta\mathbf{y}^H(k)\Delta\mathbf{y}(k) \tag{3.6}$$

The three terms in this expression are generally called the "error" term, the "effort" term and the "rate" term. The variables are defined as follows: $\mathbf{e}_{des}$ is a set of desired error outputs; λ_1 is a weighting coefficient for the control signals and has the effect of preventing small reductions at the error sensors at the expense of large control signals; $\Delta\mathbf{y}(k)$ is $\mathbf{y}(k) - \mathbf{y}(k-1)$; λ_2 is a weighting coefficient that penalizes large changes in the control variables which can sometimes have a destabilizing effect on iterative algorithms. Newton's algorithm for this cost function thus becomes:

$$\mathbf{y}(k) = (1 - \mu\lambda_1)\mathbf{y}(k-1) - \mu\lambda_2[\mathbf{y}(k-1) - \mathbf{y}(k-2)] - \mu\mathbf{C}^{-1}[\mathbf{e}(k-1) - \mathbf{e}_{des}] \tag{3.7}$$

Modal solution

Let us define a spatial modal vector as:

$$\mathbf{V}_m = \frac{1}{\sqrt{N}}\begin{Bmatrix} 1 \\ e^{j(\frac{2\pi m}{N})} \\ \cdots \\ e^{j(\frac{2\pi m}{N})(N-1)} \end{Bmatrix} \tag{3.8}$$

where m is the circumferential mode order and N is the number of actuators and sensors evenly positioned around the duct. The spatial modal vectors $\mathbf{V}$ are orthogonal and satisfy the following relationship:

$$\mathbf{V}_l^{\mathrm{H}}\mathbf{V}_m = \begin{cases} 0 & \text{for } l \neq m \\ 1 & \text{for } l = m \end{cases} \tag{3.9}$$

where l and m are integers smaller than N.

The output vector from the microphone array in the duct can be written as a summation of several modes:

$$\mathbf{e}(k) = \sum e_l(k)\mathbf{V}_l \tag{3.10}$$

where e_l is a complex number representing lth modal coefficient.

Since the primary goal is to control one single circumferential mode (m = 6), the output from the controller to the actuator can be expressed as

$$\mathbf{y}(k) = y_M(k)\mathbf{V}_M \tag{3.11}$$

where $y_M(k)$ is a complex number representing the modal controller output at the kth iteration.

In Newton's algorithm, the system transfer function **C** has to be provided to update the input to the actuators. The easiest way to measure the transfer function is to send a signal to the actuators and to measure the microphone outputs without the primary noise sources.

The calibration input to the actuator is given by

$$\mathbf{y}_{cal} = y_{cal}\mathbf{V}_M \tag{3.12}$$

where y_{cal} is the calibration level. If the mth mode is generated and propagated through the duct, the microphones output can be expressed as

$$\mathbf{x}_{cal} = x_{cal}\mathbf{V}_M \tag{3.13}$$

where x_{cal} is the modal coefficient of the microphone outputs. Therefore, the transfer function can be easily calculated as:

$$\mathbf{C} = \mathbf{x}_{cal}/\mathbf{y}_{cal} = (x_{cal}/y_{cal})\frac{\mathbf{V}_M}{\mathbf{V}'_M} = C_M\mathbf{V}_M\mathbf{V}_M^{\mathbf{H}} \tag{3.14}$$

where $C_M = x_{cal}/y_{cal}$ is mth modal transfer function coefficient. Its inverse is given as

$$\mathbf{C}^{-1} = \mathbf{y}_{cal}/\mathbf{x}_{cal} = (1/C_M)\mathbf{V}_M\mathbf{V}_M^{\mathbf{H}} = C_M^{-1}\mathbf{V}_M\mathbf{V}_M^{\mathbf{H}} \tag{3.15}$$

By multiplying both sides of equation (3.7) by the modal vector $\mathbf{V}_M$, we get:

$$\mathbf{V}_M^{\mathbf{H}}\mathbf{y}(k) = (1-\mu\lambda_1)\mathbf{V}_M^{\mathbf{H}}\mathbf{y}(k-1) - \mu\lambda_2\mathbf{V}_M^{\mathbf{H}}[\mathbf{y}(k-1)-\mathbf{y}(k-2)] - \mu\mathbf{V}_M^{\mathbf{H}}\mathbf{C}^{-1}[\mathbf{e}(k-1)-\mathbf{e}_{des}]$$

By substituting equations (3.10), (3.11) and (3.15) in the expression above and using the orthogonal properties of the modal vectors (3.9), the above vector equation can be simplified to the following scalar equation:

$$y_M(k) = (1-\mu\lambda_1)y_M(k-1) - \mu\lambda_2[y_M(k-1)-y_M(k-2)] - \mu C_M^{-1}[e_M(k-1)-e_{des\,M}] \tag{3.16}$$

3.2.3. Sensor and Actuator Calibration

Actuator calibration

Since we want to generate a single spatial mode from the actuator array, any difference among the actuator channels (both in amplitude and phase) must be compensated. These differences can be caused by differences between the actuator mechanical and electronic elements. The compensation process can implemented as shown in Figure 3.3:

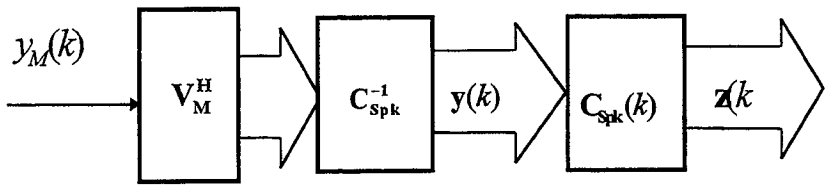

Figure 3.3. Actuator calibration - Block diagram

$\mathbf{z}(k)$ and $\mathbf{y}(k)$ represent the complex vectors from the actuator surface sensors and from the controller output, respectively. The nth element of the inverse transfer function vector $\mathbf{C}_{spk}^{-1}$ can then be calculated by

$$C_{spk}^{-1}(n) = y(n) / z(n); \qquad n = 1,\ldots,N \tag{3.17}$$

where $y(n)$ and $z(n)$ are nth element of the $\mathbf{y}$ and $\mathbf{z}$ vectors, respectively. Since the PZT actuator exhibits some non-linearity, the transfer function will be a function of the control level. Therefore, $\mathbf{C}_{spk}^{-1}(l)$ should be measured on-line so that the actuator gain and phase variation can be compensated at all times.

Including the compensation factor, the complex output vector from the controller then becomes:

$$\begin{aligned} \mathbf{y}(k,n) &= C_{spk}^{-1}(k,n) V_M(n) y_M(k) \\ &= V_{spk}(n) y_M(k) \end{aligned} \tag{3.18}$$

where $y(k,n)$ is the nth element of the output vector $\mathbf{y}(k)$ and

$$V_{spk}(n) = C_{spk}^{-1}(k,n) V_M(n). \tag{3.19}$$

Sensor calibration

Since the exact modal information needs to be extracted from the sensor array, any difference (magnitude and phase) among sensor input channels has to be compensated.

These differences can be caused by differences between sensors and sensor electronics (all the way to the controller digital input). The compensation process can be implemented as shown in the flow chart in Figure 3.4:

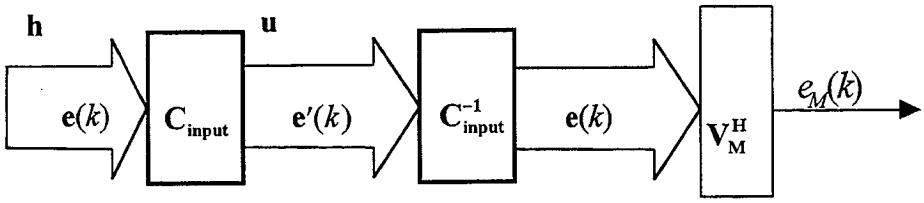

Transfer function between mics. input and input to the controller

Input gain and phase compensation (off-line)

Spatial modal decomposition

Figure 3.4. Sensor calibration - Block diagram

The symbols **h** and **u** represent the complex input vectors to the sensors and to the controller, respectively, obtained during sensor calibration. The nth element of the inverse of the input transfer function vector $\mathbf{C}_{\mathbf{input}}^{-1}$ is therefore given by:

$$C_{input}^{-1}(n) = h(n) / u(n); \qquad n = 1,\ldots,N \tag{3.20}$$

where $h(n)$ and $u(n)$ are nth element of the **h** and **u** vectors, respectively. Since the responses and gains of the sensors can be assumed to be linear and not to change during the test period, the sensor calibration can be conducted by off-line.

Since we are only interested in the mth mode, the modal error coefficient at the k^{th} iteration is given by:

$$e_M(k) = \mathbf{V}_{\mathbf{M}}^{\mathbf{H}}\mathbf{e}(k) \tag{3.21}$$

where the n^{th} element of the input error vector $\mathbf{e}(k)$ is given by:

$$e(k,n) = C_{input}^{-1}(n)e'(k,n), \qquad n = 1,\ldots,N, \tag{3.22}$$

and $e'(k,n)$ is the input to the controller from the nth error sensor.

3.2.4. Modal Control Implementation

Time-domain averaging (signal enhancement)

Time-domain averaging is used in the data acquisition process to minimize the effect of broadband noise. Time-domain averaging is possible since the test signal is periodic and stationary, and because the signal generation and acquisition processes are synchronized to the blade passage frequency through a shaft encoder (synchronous sampling). Time-domain averaging is implemented iteratively as follows:

$$\bar{x}(blck,n,i) = \bar{x}(blck-1,n,i)\frac{blck-1}{blck} + x(blck,n,i) \qquad \begin{matrix} blck = 1,\ldots M \\ n = 1,\ldots N \\ i = 1,\ldots I \end{matrix} \tag{3.23}$$

$$= \text{Ave\_T}[x(blck,n,i)]$$

where Ave_T[ ] is a time-domain averaging operator, x is a discrete time series, $\bar{x}$ is an average time series, *blck* is the data block counter, n is the channel number, and i is the sample counter in each data block.

Fourier transform of single frequency data

The basic equations for the DFT (forward and inverse transforms) are:

$$X(k) = \frac{1}{I}\sum_{i=0}^{I-1} x(i) e^{-j\frac{2\pi ki}{I}} \tag{3.24}$$

$$x(i) = \sum_{k=0}^{I-1} X(k) e^{j\frac{2\pi ki}{I}} \tag{3.25}$$

A matrix representation of Equation (3.24) for $N = 8$ is given by:

$$\begin{Bmatrix} X(0) \\ X(1) \\ X(2) \\ X(3) \\ X(4) \\ X(5) \\ X(6) \\ X(7) \end{Bmatrix} = \frac{1}{8}\begin{bmatrix} 1 & 1 & 1 & 1 & 1 & 1 & 1 & 1 \\ 1 & e^{-j\frac{\pi}{4}} & -j & e^{-j\frac{3\pi}{4}} & -1 & -e^{-j\frac{\pi}{4}} & j & -e^{-j\frac{3\pi}{4}} \\ 1 & -j & -1 & j & 1 & -j & -1 & j \\ 1 & e^{-j\frac{3\pi}{4}} & j & e^{-j\frac{\pi}{4}} & -1 & -e^{-j\frac{3\pi}{4}} & -j & -e^{-j\frac{\pi}{4}} \\ 1 & -1 & 1 & -1 & 1 & -1 & 1 & -1 \\ \cdots\cdots & & & & & & & \\ & & & & & & & \\ & & & & & & & \end{bmatrix}\begin{Bmatrix} x(0) \\ x(1) \\ x(2) \\ x(3) \\ x(4) \\ x(5) \\ x(6) \\ x(7) \end{Bmatrix}$$

If an FFT algorithm is implemented, the total number of multiplications performed is equal to $N\log_2 N$. However, since we are only interested in a single frequency component, a direct calculation of that Fourier component based on the DFT is more efficient than using the FFT algorithm.

For a single frequency Fourier coefficient, the total number of multiplication using the DFT is N. The direct DFT approach can be implemented as follows:

$$X_L = \frac{1}{I}\sum_{i=0}^{I-1} x(i) e^{-j\frac{2\pi Li}{I}} = \text{SDFT}[x(i)] \tag{3.26}$$

where SDFT[ ] is a discrete Fourier transform of a single frequency data, X_L is the Fourier coefficient, and L is the number of period in each block sample data. The time series $x(i)$ can be reproduced from the Fourier coefficient X_L as:

$$x(i) = \mathrm{Re}(X_L e^{j\frac{2\pi Li}{I}}), \quad i = 0,\ldots,I-1 \tag{3.27}$$

3.2.5. Modal controller implementation - Summary

Figure 3.5 shows a signal flow block diagram for the entire system including controller, signal conditioning, and acoustic paths. The computations required to generate the controller output are outlined below:

Input adaptive control parameters: λ_1, λ_2, μ.

i. Calibration - Sensors and actuators

Sensor calibration (off-line):

$$C_{input}^{-1}(n) = h(n)/u(n), \quad n = 1,\ldots,N. \tag{3.28}$$

where $u(n)$ = SDFT[Ave_T[$u(blck,n,i)$]] and $h(n)$ = SDFT[Ave_T[$h(blck,n,i)$]] are the frequency-domain input and output calibration data, respectively.

Actuator calibration (off-line and on-line)

$$C_{spk}^{-1}(k,n) = y(k,n)/z(n), \quad n = 1,\ldots,N. \tag{3.29}$$

where $y(k,n)$ is an output from the controller to an actuator and $z(n)$ = SDFT[AVE_T[$z(blck,n,i)$]] is a frequency-domain actuator output.

ii. Off-line system identification

$$C_M^{-1} = y_{M_{cal}} / e_{M_{cal}}, \tag{3.30}$$

where $e_{M_{cal}}$ is the spatial modal coefficient of the input signal during calibration when the fan noise is off ($\mathbf{d}(t) = 0$) (calculated using equations (3.33) to (3.35).

iii. Calculation of modified spatial modal vectors

Modified spatial modal vector for input sensors

$$\begin{aligned} V_{sen}(n) &= C_{input}^{-1}(n) V_M^n(n) \\ &= C_{input}^{-1}(n) e^{-j\frac{2\pi(n-1)M}{N}} / \sqrt{N} \quad n = 1,\ldots,N \end{aligned} \tag{3.31}$$

where $C_{input}^{-1}(n)$ is given in equation (20).

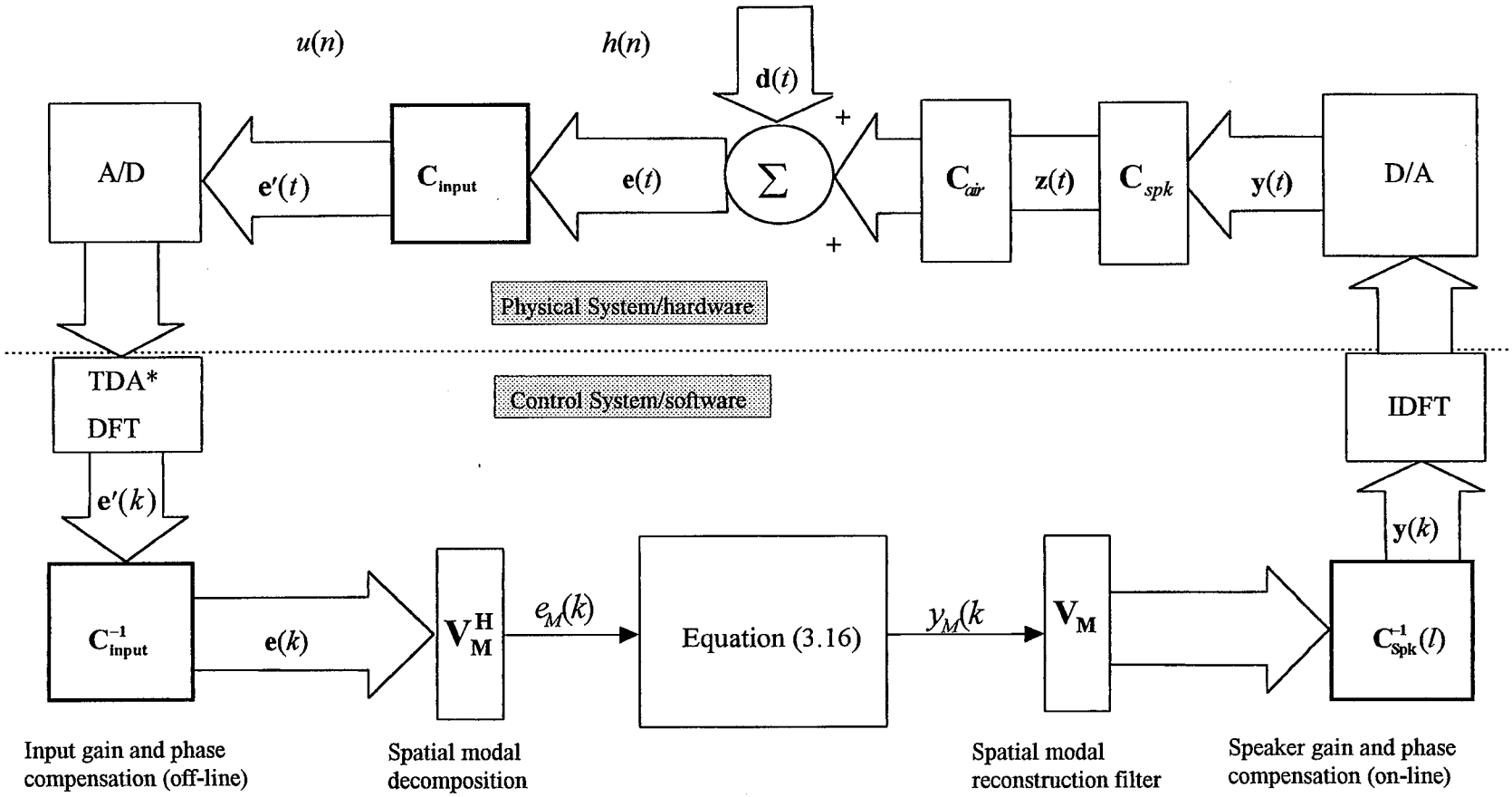

TDA: Time Domain Average

Figure 3.5. Modal control system - Signal flow block diagram

Modified spatial reconstruction modal vector for actuators

$$\begin{aligned} V_{spk}(n) &= C_{spk}^{-1}(n)V_M(n) \\ &= C_{ispk}^{-1}(n)e^{j\frac{2\pi(n-1)}{N}}/\sqrt{N} \qquad n=1,\ldots,N \end{aligned} \tag{3.32}$$

where $C_{spk}^{-1}(n)$ is given in equation (3.17).

iv. Time Domain Average

$$\bar{e}(blck,n,i) = \text{Ave\_T}[e(blck,n,i)] \qquad \begin{matrix} blck=1,\ldots M \\ n=1,\ldots N \\ i=1,\ldots I \end{matrix} \tag{3.33}$$

where *blck* is the data block counter, n is the input channel number and i is the data sample counter in each data block.

v. Fourier Transform

Lets define $e(k,n,i)$ to be the averaged error input data at the k^{th} iteration. Its Fourier transform is then given by:

$$e(k,n) = \frac{1}{I}\sum_{i=0}^{I} e(k,n,i)e^{-j\frac{2\pi Li}{I}}, \qquad n=1,\ldots,N \tag{3.34}$$

where L is the number of periods included in each block sample data. In the case of $I=4$ and $L=1$,

$$e(k,n) = \{e(k,n,0) \quad e(k,n,1) \quad e(k,n,2) \quad e(k,n,3)\}\begin{Bmatrix} 1/4 \\ -j/4 \\ -1/4 \\ j/4 \end{Bmatrix}, \qquad n=1,\ldots,N$$

vi. Spatial modal decomposition

$$e_M = \sum_{n=1}^{N} V_{sen}(n)e(k,n) \tag{3.35}$$

vii. Modal output coefficient update

$$y_M(k+1) = (1-\mu\lambda_1)y_M(k) - \mu\lambda_2[y_M(k) - y_M(k-1)] - \mu C_M^{-1}e_M(k) \tag{3.36}$$

viii Spatial modal reconstruction

$$y(k+1,n) = V_{spk}(n)y_M(k+1), \quad n=1,\ldots,N \tag{3.37}$$

ix. Time series output

$$y(k+1,n,i) = \mathrm{Re}[y(k+1,n)e^{j\frac{2\pi Li}{I}}], \qquad \begin{matrix} i = 0,\ldots,I-1 \\ n = 1,\ldots,N \end{matrix} \tag{3.38}$$

3.3. Controller Software Functionalities

Calibration - Transfer function measurement:

- Plate radiators and error microphones - 16x16, off-line calibration
- Plate radiators and actuator feedback sensor - both on-line and off-line calibration
- Reference microphone and error microphones or calibration signal and control microphones (off-line calibration).

Processing

Generate transfer functions and their inverse

Control

- Manual control: Manually adjust the phase and amplitude of the canceling mode.
- Feedforward control: adapt the output based on microphone input data and modal transfer function.
- Feedback control: compensate for phase and sensitivity changes of the array elements by measuring the transfer function between the control outputs and the array elements.
- Display control microphone performance index
- Display amplitude and phase of modal input and output signals
- Software protection - Shut down controller if performance goes below a specific level (e.g. -5 dB).
- Gain control - Limit the output level.

Controller Read and Write

a) Input

- m-order of mode to be canceled
- Adaptive control parameters: λ_1, λ_2, μ.
- Block average number
- Control microphone sensitivity and phase.
- Actuator sensitivity and phase.
- Inverse transfer functions.

b) Output

- Actuator and microphone levels during operation.

3.4. Controller Hardware

A schematic of the controller hardware is shown in Figure 3.6.

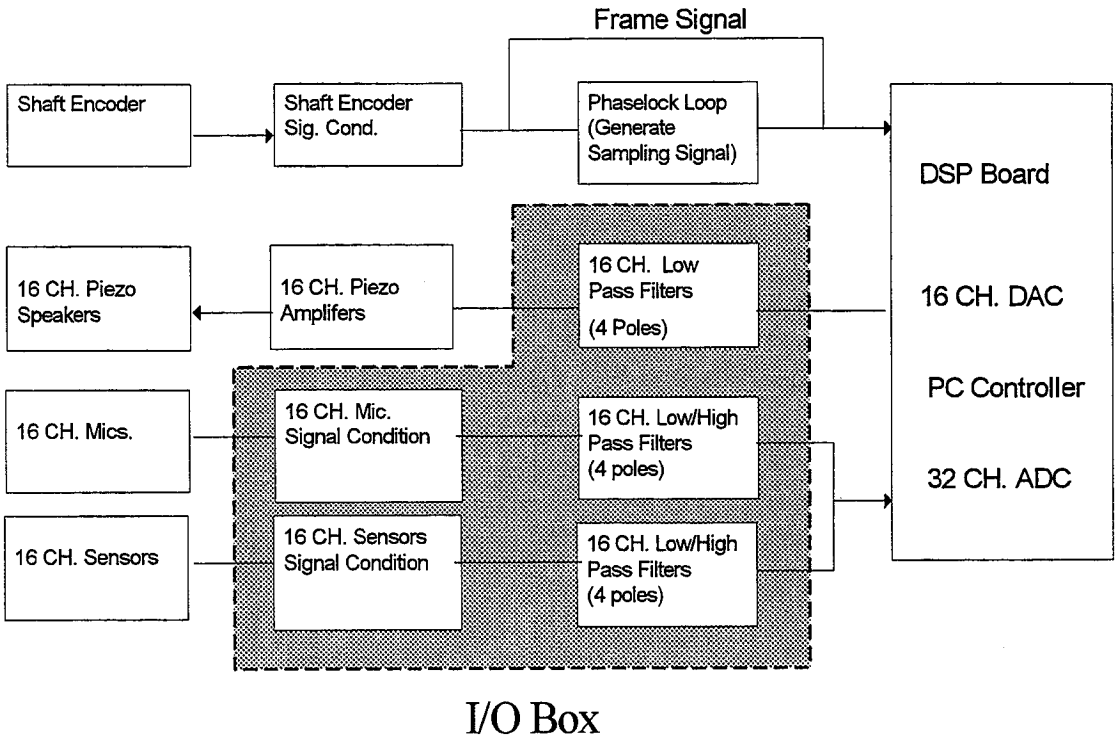

Figure 3.6 Schematic of ANC controller and signal conditioning hardware.

Controller and signal conditioning specifications

- Cut-off frequency for input band-pass filters: 800 to 1.2 KHz.
- Cut-off frequency for output low-pass filters: 1.2 KHz.
- PC-based controller with off-the-shelf hardware
- 12-bit, ADC/DAC I/O boards with sampling rate of at least 4 KHz for 16 channels
- Externally-triggered ADC sampling and DAC conversions
- Floating point DSP board with 40 MFLOPS or higher performance (40 MHz clock speed).
- Maximum frequency to be controlled (2BPF): 1 KHz
- Maximum Sampling Frequency: (4 x 2BPF): 4 KHz.

The second version of the control software was delivered to GE CRD by Penn State. The control software consists of about 5,000 lines of codes, with roughly half the code written in C and the other half written in assembly language.

Controller hardware/software implementation

The controller hardware includes an industrial rack mount 486-DX2-66 PC, a Motorola DSP96002 signal processing board, a 32-channel ADC input board, and a 16-channel DAC output board. Conventional peripherals are part of the system such hard and floppy drives, keyboard and monitor.

The software was implemented by Dr. Scott Sommerfeldt and Dr. Yong-Cheol Park from the Pennsylvania State University. The software includes approximately 5,000 lines of code, half written in C, and the other half written in 96000 Assembly language. The software has the functionalities listed in Section 3.3. The software has a user-friendly, menu-driven interface which allows the easy setup of important control parameters such as the m-order of the mode to be canceled, convergence constants. The user can also operate the system either in a manual or an automatic mode and start the various calibration procedures from the menu interface. Live displays of individual signals, modal signals, and performance indexes are available for use during the testing process.

The entire system was tested at GE CRD using a laboratory setup composed of 16 audio speakers generating a pseudo $m = 4$ mode "primary noise" at a frequency around 930 Hz. The 16-actuator array was mounted near the 16 audio speakers with the 16-microphone array placed between the primary noise source and the control actuator array.

Shaft encoder signal

The speed of rotation of the shaft is obtained using an optical encoder. The encoder signal is used to generate a "frame signal" at the 2BPF (around 1 KHz) which is used as an absolute frame reference and to initialize the controller. A sampling signal at 4 times 2BPF is derived from the frame signal using an off-the-shelf frequency multiplier in order to synchronously trigger the data input and output processes.

Input/Output signal conditioning box

A custom-designed I/O signal conditioning box was used for this test. It includes 16 inputs for the microphone array, 16 inputs for the feedback sensors on the array elements, and 16 outputs for the canceling array. The I/O box performs the following functions:

- 32-input microphone signal conditioning including on all channels: microphone preamplifier and power supply, 0-40 dB adjustable gain, and active 4-pole low-pass and high-pass filters programmable using plug-in resistor packs.
- 16-output array element signal conditioning including on all channels: adjustable gain and active 4-pole low-pass reconstruction filter programmable using plug-in resistor packs.

Additional specifications include: SNR greater than 48 dB, cross-talk less than -48 dB, and Common Mode Rejection Ratio (CMRR) greater than 80 dB, test-channel output with dial-in channel selector, connector for ribbon cable to I/O boards in the ANC controller.

Amplifier array

The amplifier array consists of 8 stereo audio amplifiers with custom step-up transformers and impedance matching inductors to drive the PZT elements.

4. System Integration

This section describes the ANC system and its integration to the NASA fan duct. A schematic of the entire ANC system integrated in the NASA fan is shown in Figure 4.1.

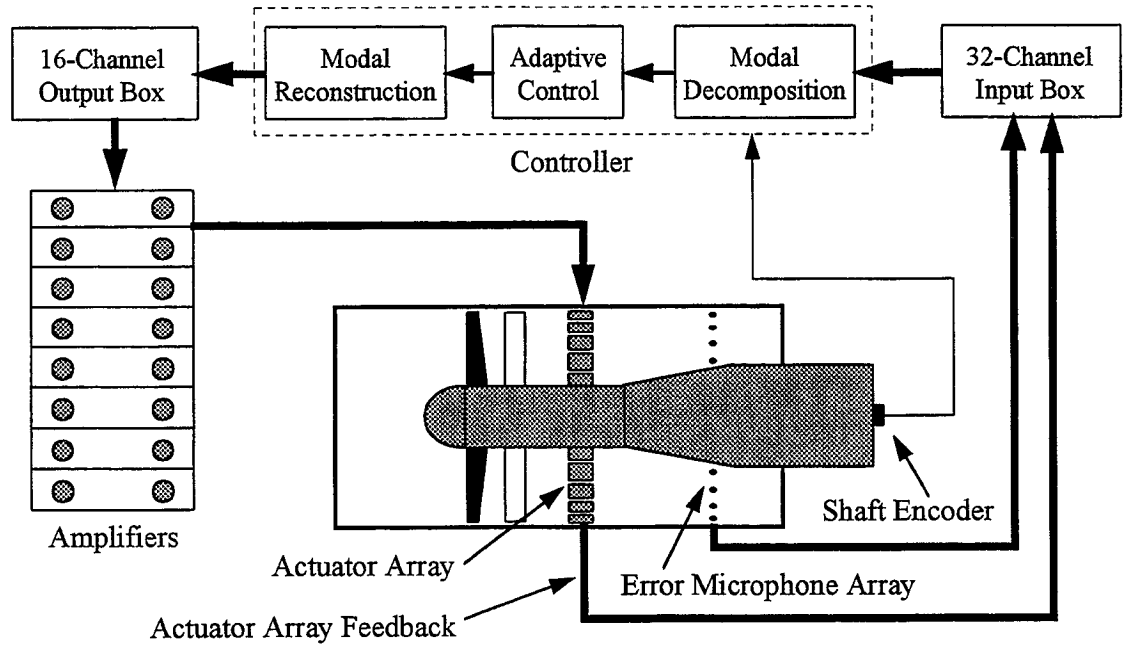

Figure 4.1. System Diagram

4.1. Actuator Array Integration

The actuator array was mounted on a 12-inch long spool section of the NASA fan duct. Flats were machined on the spool to mount each array element. Each element was resiliently mounted on the ring using a 4-bolt pattern torqued to 30 in-lb for easy mounting and removal. A schematic of the ring source actuator design is shown in Figure 4.2.

Testing was performed to determine the amount of structure-borne cross-talk between actuators—that is, the excitation of one actuator by its neighbors through structure-borne vibrations. Initial results showed an unacceptably high amount of cross-talk (-10 dB) between adjacent actuators primarily as a result of the matching resonances between actuators, the low damping of the diaphragms, and the low resiliency of the initial mounting technique. The problem was resolved by doubling the thickness of the vibration isolation gasket, putting a tygon jacket around each mounting screw, and using vibration absorbers between the actuator frame and the mounting bolt.

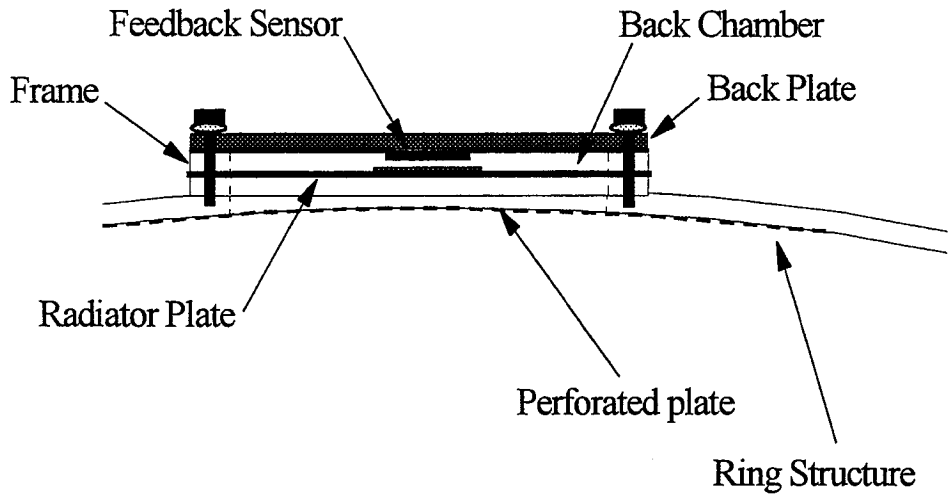

Figure 4.2. Ring source actuator design schematic.

A 30-mil perforated steel plate was cut to dimension to fit into a 30-mil 5 3/16-in groove machined inside the ring spool by NASA. The perforated plate ensures smooth flow over the actuators and provides additional protection for the actuators.

4.2. Microphones

The feedback microphone array was implemented using 16 off-the-shelf Knolls microphones with custom signal conditioning circuits similar to the microphones used in the NASA Fan rotating rake measurement system. Calibration showed that the microphone response was accurate up to 135 dB with fairly flat amplitude and phase response over the frequency range of interest.

Each microphone in the 16-microphone array was packaged in a porous shell adapter which was flush mounted in the NASA fan ring.

4.3. Calibrator

A microphone/canceling source calibrator was designed and fabricated. The calibrator is used to perform amplitude and phase calibration of each microphone and canceling source up to a frequency of 3 KHz using a Shroeder calibration sequence. The calibrator consists of a plastic housing with a circular piezoceramic bender element generating the calibration acoustic signal and separating the calibrator in two chambers.

The calibration process was designed to compensate the amplitude and phase differences among 16 input sensor and 16 output channels. The calibration process was implemented in the following way:

1. Calibrate the feedback microphones in the back chambers of the actuators.

   A calibration signal was sent to each actuator from the controller to drive the actuator in the selected frequency range. A transfer function was measured between every feedback microphone and the microphone inside the calibrator (as a reference). Each feedback microphone input was multiplied by the inverse of its transfer function to compensate for the phase and amplitude differences among all channels.

2. Calibrate the actuators using the feedback microphones.

   A calibration signal was sent to each actuator from the controller to drive the actuator in the selected frequency range. A transfer function was measured between the calibration signal (as a reference) and each feedback microphone input (microphone sensitivity and phase was compensated). Each actuator output was multiplied by the inverse of its transfer function to compensate for the phase and amplitude differences among all channels during controller operation.

3. Calibrate the input sensors.

   A calibration signal was sent to the calibrator from the controller to drive each actuator in the selected frequency range. A transfer function was measured between the control microphone and the microphone inside the calibrator (as a reference). Each feedback microphone input was multiplied by the inverse of its transfer function to compensate for the phase and amplitude differences among all channels during controller operation.

The speaker calibration process was initially designed to compensate for actuator sensitivity and phase variation among all channels for both on-line and off-line operation. This procedure was instituted when it was observed that actuator sensitivity varied with different input levels for an initially-selected PZT material. A feedback sensor was designed to monitor the sensitivity change during operation and to allow on-line compensation. It was found that actuator non-linearity was not an issue when using the final selection for PZT material, and, combined with the difficulty of implementing on-line calibration within the tight test schedule, it was decided not to implement on-line calibration in the software, and the calibration was accomplished off-line as described above.

The first resonance frequency of the piezoceramic bender element is around 900 Hz. It can be driven by an audio amplifier or directly from a signal generator. A reference microphone is mounted in the front calibration chamber facing the opening. An O-ring on the chamber opening allows airtight contact between the calibration chamber and the sensor or actuator being calibrated. Tests conducted with an instrumentation microphone showed that the transfer function (both magnitude and phase) between the reference microphone and the calibration microphone was flat up to around 3 KHz.

5. Results

This section describes the test results obtained with the GE ANC system mounted in the NASA Active Noise Control Fan (ANCF) facility.

5.1. Test Bed

The GE ANC Modal Control System was tested installed in the NASA Lewis Research Center's (LeRC) 48 inch ANCF facility.[3] The ANCF uses a 16-bladed variable-pitch rotor and can be configured with stator vanes to provide specific mode generation and propagation for Active Noise Control Research.

A unique feature on the ANCF is the direct attachment of the rotor centerbody to the rig support column, eliminating the need for struts, which could contaminate acoustic measurements. Additionally, an Inflow Control Device (ICD) allows for static testing.

The combination of low tip speed (~400 ft/sec) and the 48 inch diameter produces fan tones of the same frequencies produced by full size advanced engines. The ANCF is constructed of component spool pieces which can be replaced by ANC systems to be tested.

The primary measurement device on the ANCF is the Rotating Rake. The Rotating Rake is an implementation of a technique originally conceived by T.G. Sofrin [4] whereby a rake containing radially-distributed pressure transducers rotates in the circumferential direction at a precise fraction of the fan rotational speed. Since each circumferential acoustic mode is known to rotate at a unique frequency [5] in the rotor reference frame , a Doppler shift is induced in the rake reference frame. Further reduction of the data into radial modes is accomplished through a least squares curve fit [6].

The ANCF is located in the NASA LeRC's Aeroacoustic Propulsion Laboratory [7] (AAPL), a hemispherical anechoic (to 125 Hz.), test facility. Farfield measurements are taken from 28 microphones at a radius of 50 feet in the ANCF horizontal plane. The SPL data from these microphones are corrected to 40 ft, standard day conditions.

5.2. Test Conditions

The test of the GE ANC system occurred over the period of July to September 1995. The primary ANC Ring configuration was the exhaust installation. The primary ANCF configuration was 26 vanes with a blade pitch of 50°. The spacing between the rotor trailing edge and the stator leading edge, measured at the hub, was 2.25 inches. The system was tested over a fan corrected RPM range of 1585 to 1804. With 16 blades and 26 vanes, the BPF is cutoff over this range.

At 2BPF, in the exhaust, the (6,0) mode begins to propagate at 1222 corrected RPM and the (6,1) mode propagates at and above 1845 corrected RPM. Therefore, in the target configuration, only a single mode propagates over the range tested. The ANC control system was designed to target the 2BPF tone and thus operated over a frequency range of 860 Hz to 980 Hz. Secondary studies were done with the ANC ring installed in the inlet.

In addition, one study was done with the ring in the exhaust, with 28 stator vanes, over a fan corrected RPM range of 1481 to 1704. At 2BPF the (4,0) and (4,1) modes are cut-on.

5.3. Data Summary

Reduced data obtained with the rotating rake are presented in the following figures. A data point was taken at a given RPM with the control on, followed by a data point with the control off.

The control off and control on power levels in the (6,0) mode versus corrected RPM are shown in Figure 5.1. The general control off levels are around 112 dB PWL, dropping to 105 dB PWL at 1800 RPM. A reduction of at least 15 dB occurs over the entire RPM range tested. The results are particularly outstanding around the design frequency of 920 Hz., with 25-30 dB PWL reduction. This implies cancellation of the entire mode. The hatched area represents very low pressure levels, where the measurements levels are less certain.

Figure 5.2 shows the results are again excellent around the 920 Hz with the ANC ring installed in the inlet. Complete cancellation of the mode occurs. Above 1720 RPM the transducer output reached the maximum safe output allowed for this test and therefore the optimum reduction could not be achieved.

When using a single ring, bi-directional propagation naturally occurs. Figure 5.3 shows the effect of the mode created by the ANC source generated in opposite propagation direction superposed with the fan mode. With the ANC system installed in the exhaust, and rake measurements obtained in the inlet, the change in mode power varied from an increase of 5 dB to a 1 dB decrease. With the system in the inlet, and the propagation in the exhaust measured, a decrease of up to 4 dB occurs, over a narrower RPM range. Of course this is highly dependent upon physical and acoustic dimensions, such as spacing between the primary source and canceling source, and propagation wavelengths.

The 2BPF total tone power (PWL) reduction is shown in Figure 5.4. The total tone power is the sum of the power of all modes in a given harmonic and direction. Each set of runs, or test date in the legend, represents a different calibration. A general trend of 4 to 8 dB total PWL reduction, with a maximum of 9 dB reduction is seen in the exhaust.

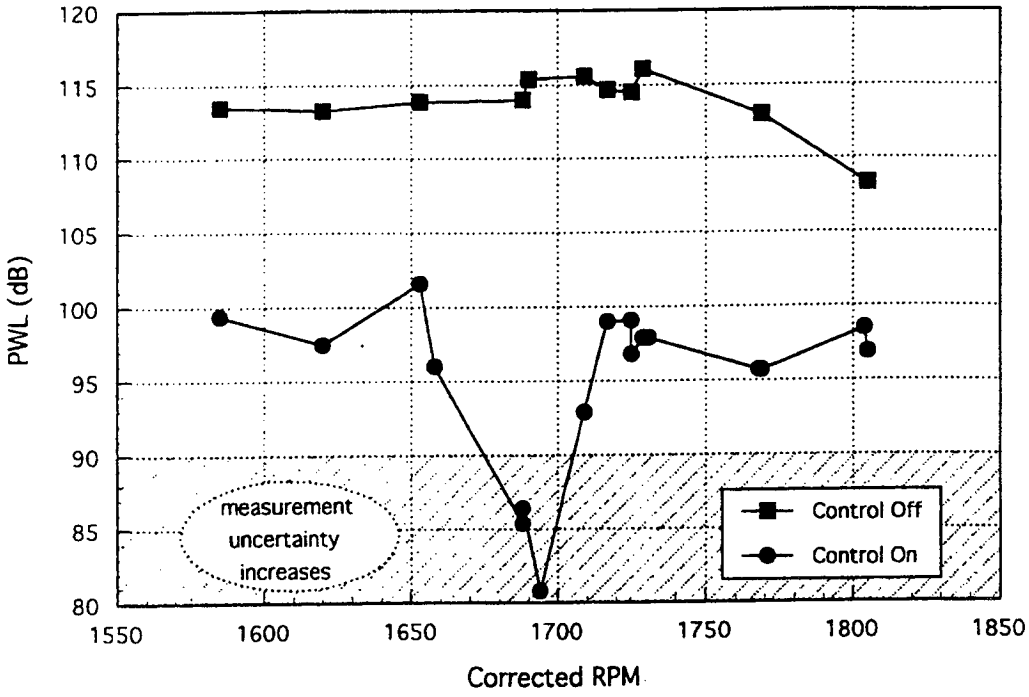

Figure 5.1 Mode (6,0) power levels in exhaust

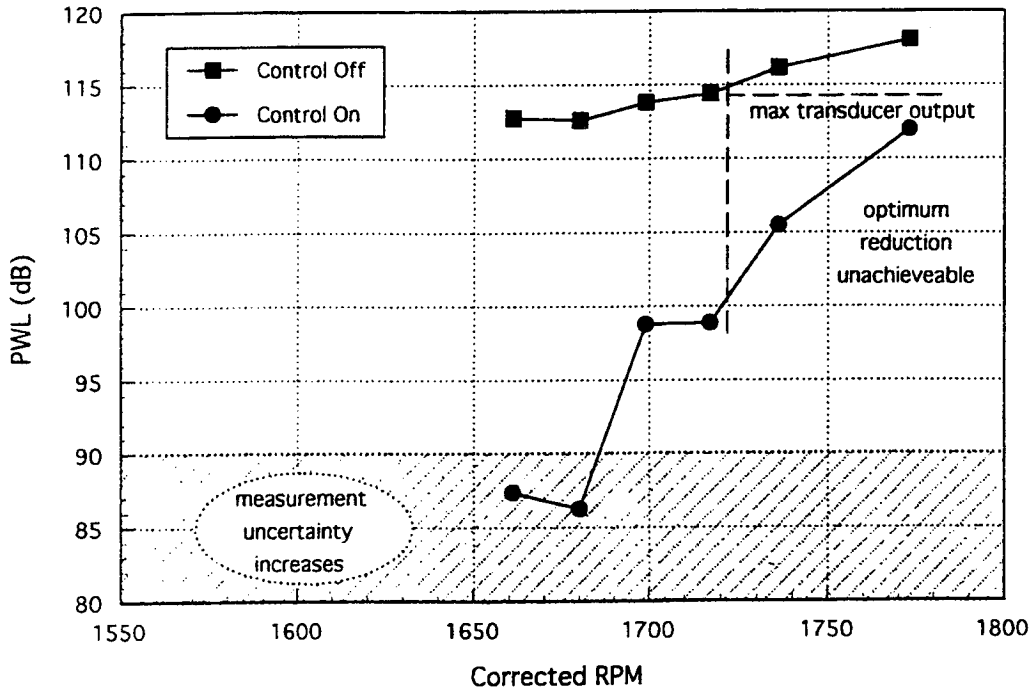

Figure 5.2 Mode (6,0) power levels in inlet

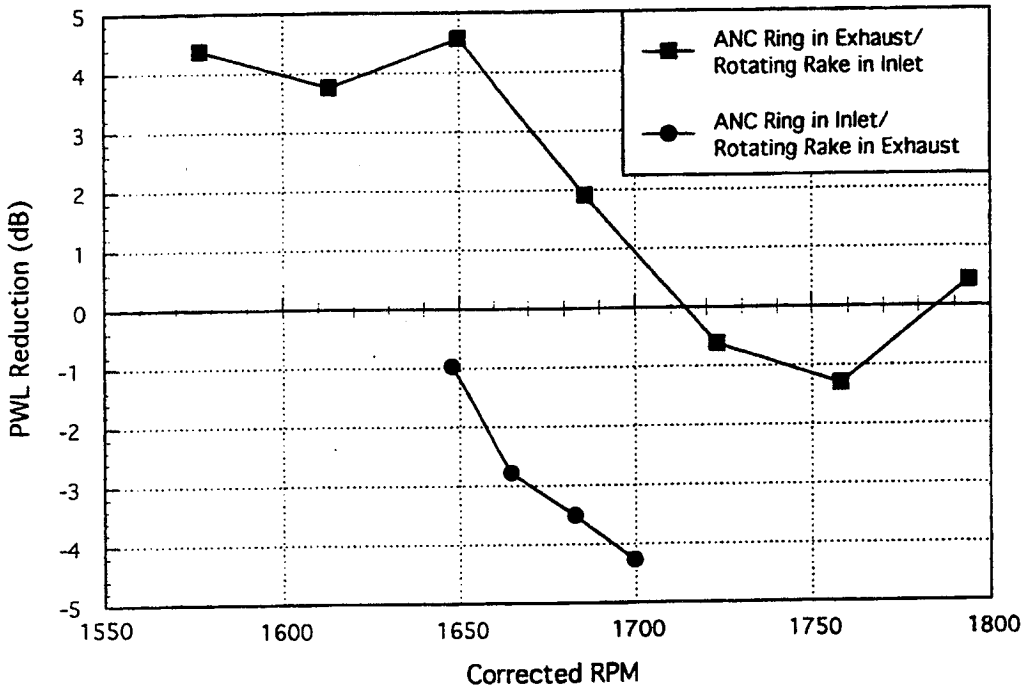

Figure 5.3 Mode (6,0) power level for opposite direction propagation

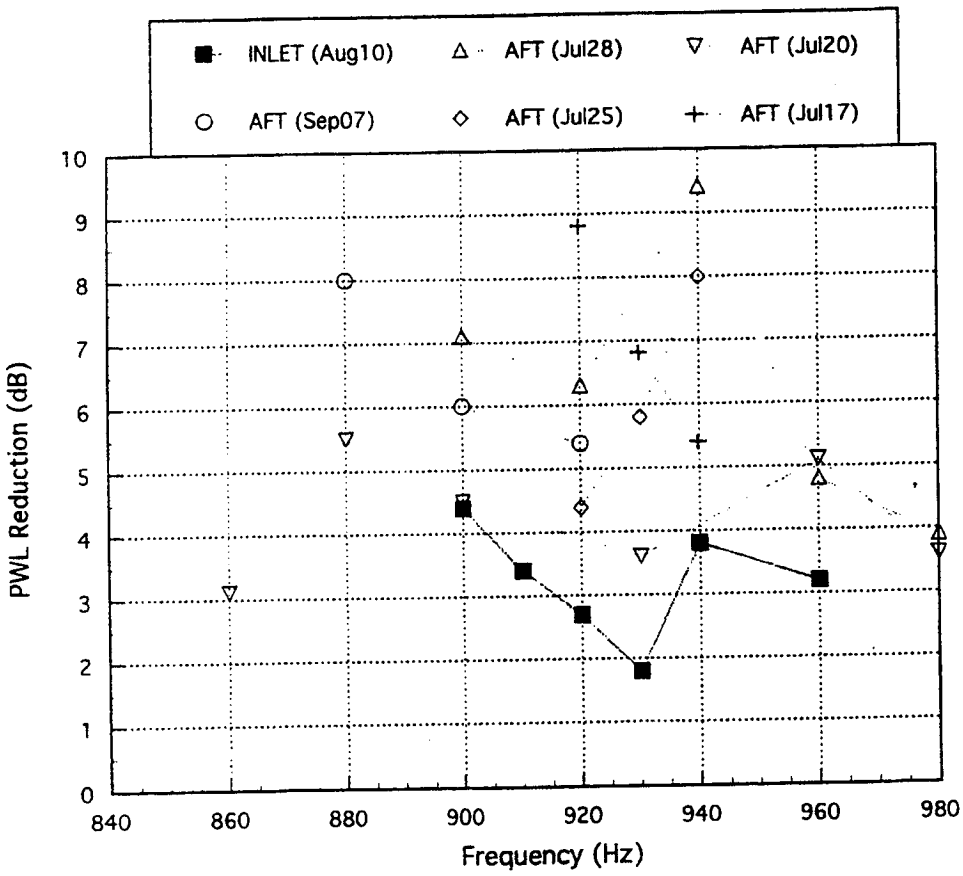

Figure 5.4 Reduction in total tone power levels

The single run taken with the ANC ring in the inlet shows 2 to 4 dB reduction. The difference between the levels of reduction is a result of increased modal spill-over in the cases with lower reductions. It is believed that the modal spillover is due to poor calibration.

Mode power structure obtained from the rotating rake is plotted in 3-D bar graph format with circumferential mode index along one horizontal axis, radial mode index along the other, and mode PWL as bar height. Along the back wall the total power in each circumferential mode is shown. The control off mode structure is presented in Figure 5.5. This is the acoustic characteristic of the fan at 2BPF.

Ideally, the only mode that would exist is the (6,0) due to rotor stator interaction, but, typically, neighboring modes are also excited, perhaps due to spacing or to blade-to-blade imperfections. Also, other physical obstructions can cause periodic flow disturbances which generate modes.

An example is the ICD (Inflow Control Device) which excites the m = -1 mode. The total tone power at 2BPF of 113.0 dB is the sum of each circumferential mode. This mode is not very large, but its contribution limits the PWL reduction that can be obtained by eliminating the (6,0) mode. If the (6,0) mode were totally eliminated, the remaining power would be 101.4 dB. This means the maximum reduction possible is 11 dB PWL.

The same format is shown in Figure 5.6 with the ANC system operating . The (6,0) mode has been completely eliminated, a 30 dB reduction. There are small increases in a few of the other modes. The total power is 104.2 dB, a 8.8 dB PWL reduction out of a possible 11.6 dB.

A clearer way of visualizing this result is to plot the back row of the 3-D plots, with control off and with control on, side by side. This is done in Figure 5.7. The complete elimination of mode 6 is seen. There is an increase of a few dB in the neighboring modes, i.e. 5 and 7. The next highest mode is 12 dB down. The sum of all these small increases in the other modes prevents a complete tone elimination.

Figure 5.8 shows the mode structure of a similar control off case. The (6,0) mode and the noise floor are comparable to the Figure 5.5 case.

The control-on results are not as favorable, as seen in Figure 5.9. The (6,0) mode while greatly reduced, has a small remnant. A larger problem is the more numerous and larger spillover modes. The total PWL reduction is 4.4 dB, not as high as the previous case.

The circumferential mode power levels in Figure 5.10 compare the control on and off circumferential levels in the case with higher spillover. Higher spillover mode levels do not permit as great a reduction in total power.

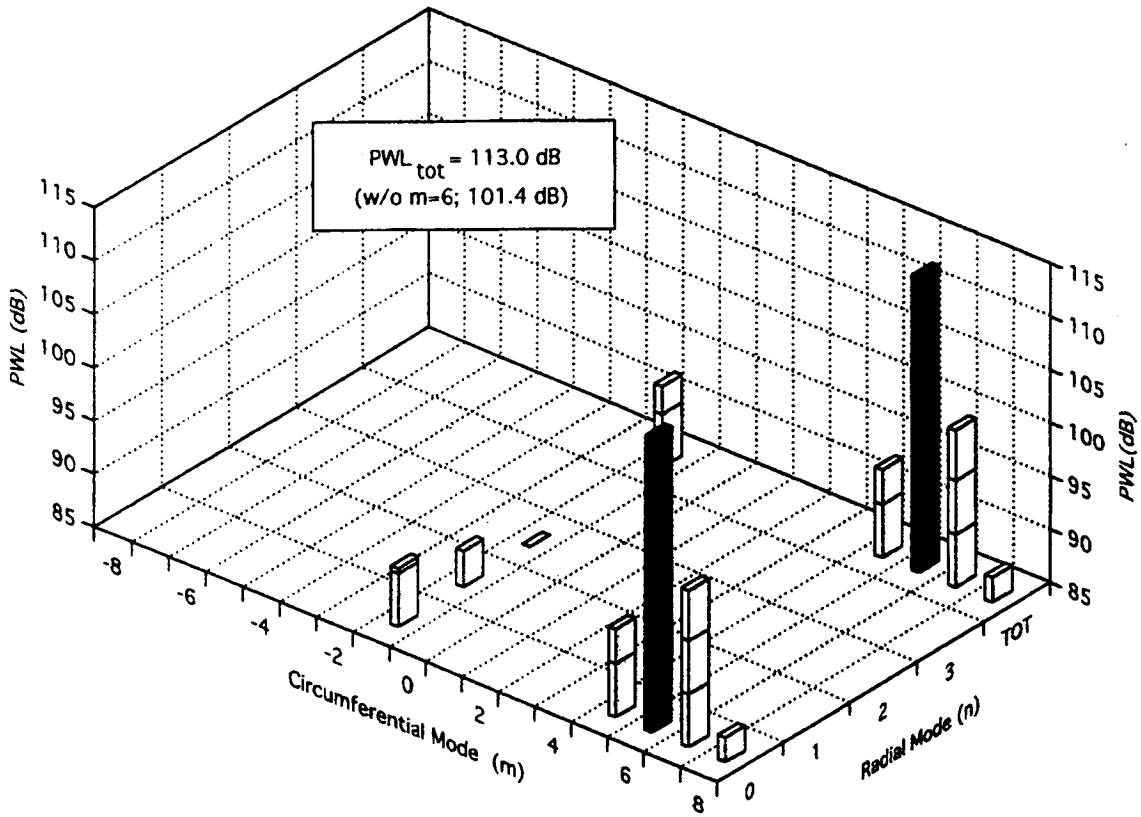

Figure 5.5 Control off mode power map. Aft, 2BPF, 1688 RPM, 920 Hz.

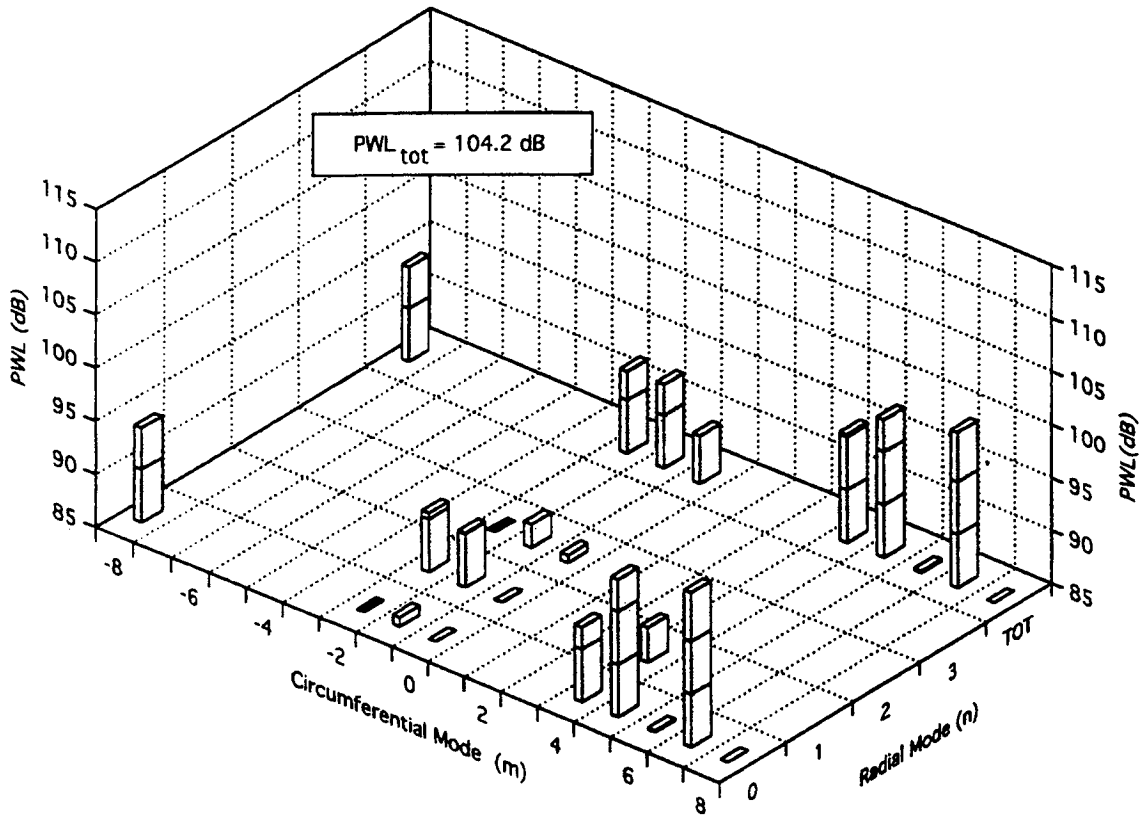

Figure 5.6 Control on mode power map (low spillover). Aft, 2BPF,1688 rpm, 920 Hz.

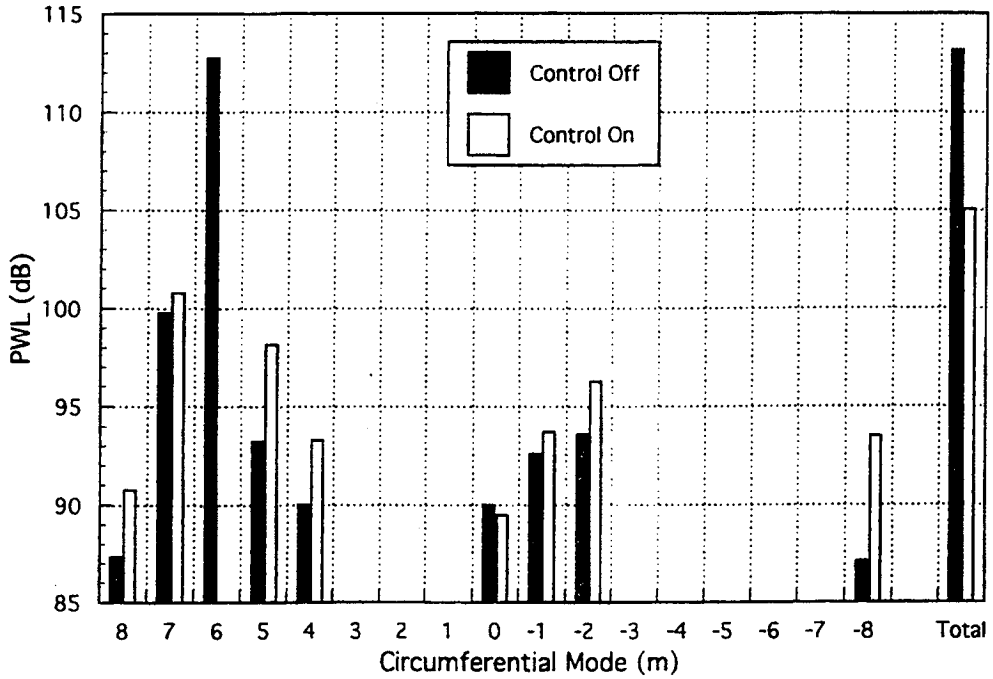

Figure 5.7 Circumferential mode power levels (low spillover). 2BPF, 1688 RPM.

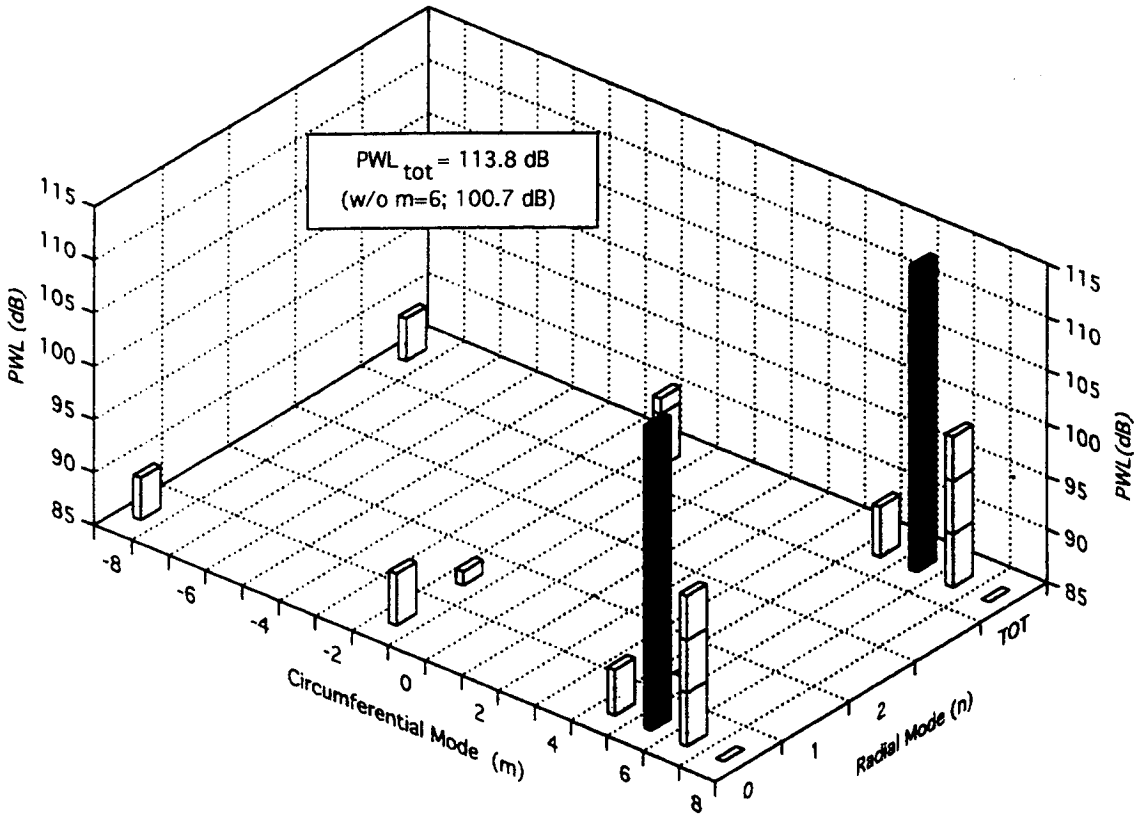

Figure 5.8 Control off mode power map. Aft, 2BPF, 1690 RPM, 920 Hz.

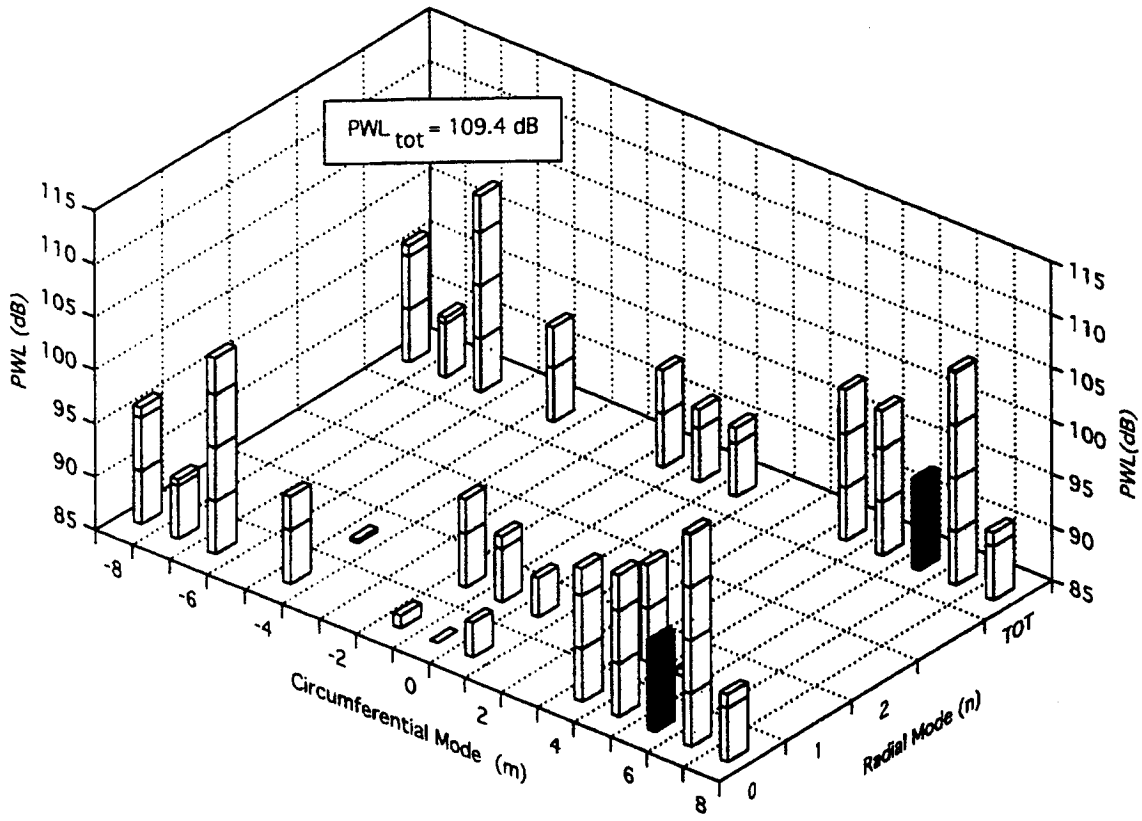

Figure 5.9 Control on mode power map. Aft, 2BPF, 1690 RPM, 920 Hz.

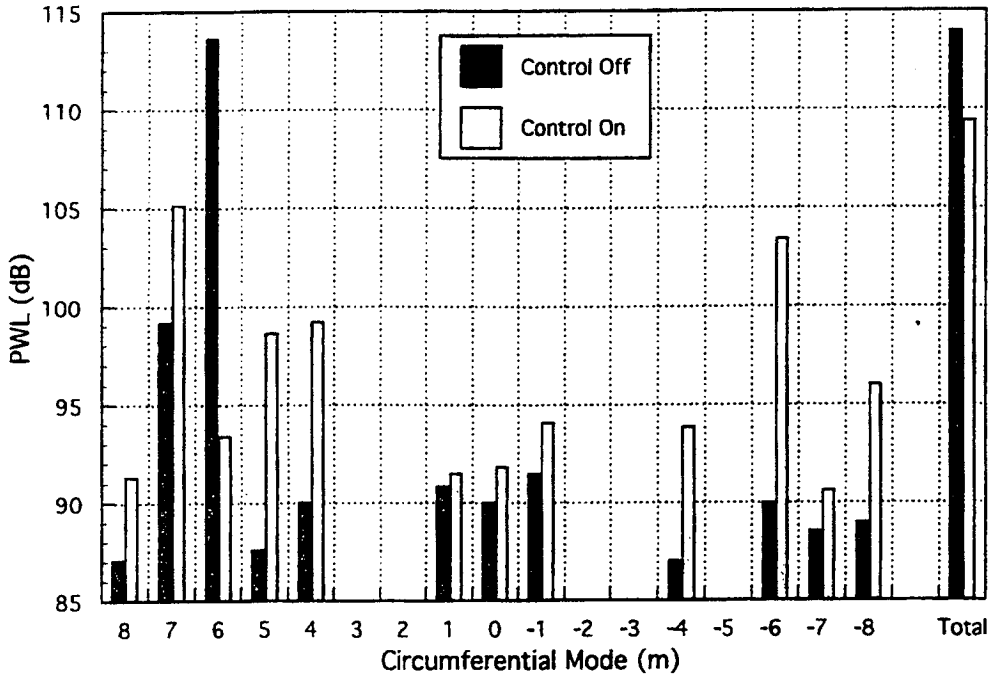

Figure 5.10 Circumferential mode power levels (high spillover). 2BPF, 1690 rpm.

A database of the complete mode structure was obtained and analyzed for each point. These two cases were chosen to represent the results. The higher levels of reduction shown in Figure 5.4 occur when the modal spill-over is low, as in Figure 5.6. Higher spill-over prevented full realization of the reduction, as seen in Figure 5.9.

The modal structure of the ANC system only, (with the fan off) is presented in Figure 5.11. The outputs of the transducers were higher than during the standard runs, in this case a 117 dB PWL. The spillover modes are generally down 15-20 dB or more. The sum of the spill-over modal power is 10 dB below the (6,0) mode. In a sense, this is the signal-to-noise ratio of the ANC system.

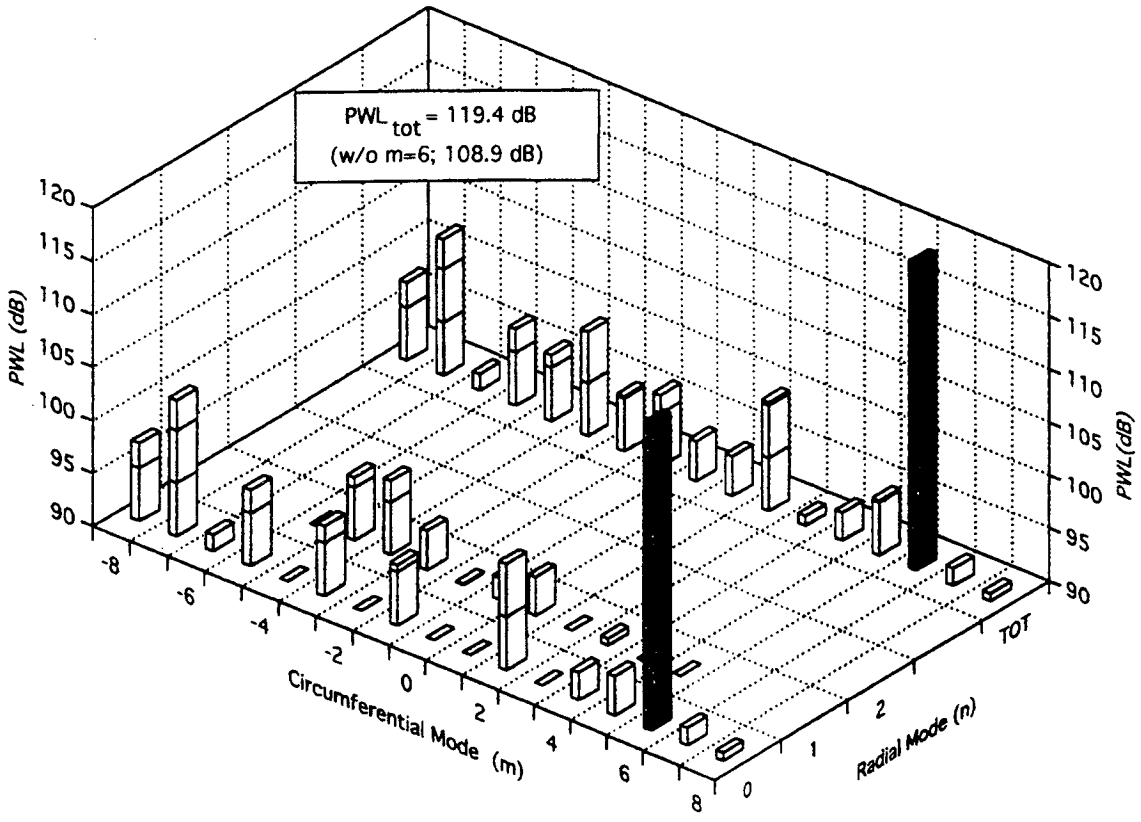

Figure 5.11 Fan off mode power map. Aft, 2BPF, 1700 RPM, 920 Hz., ANC system only

The farfield data confirm the reduction. A typical control on/off directivity comparison is shown in Figure 5.12. A 13 dB SPL reduction occurs in the (6,0) mode lobe at $\theta = 125°$. The ANC ring is installed in the aft and therefore only SPL data from $\theta = 90°$ to 180° are relevant. Integrating these two curves would yield a 2.0 dB PWL reduction. However great care must be taken with this number as the integration may not be accurate due to azimuthal variations in SPL directivity that can occur when multiple mode levels are present.

Although not designed to cancel other than $m = 6$ spinning modes, the ANC system was operated to cancel the $m = 4$ mode, which is generated when 28 stator vanes are installed in the rig. Up to 15 dB PWL reduction occurs in the total $m = 4$ mode power level as shown in Figure 5.13.

At $m = 4$, 2 radials are cut-on, the (4,0) and (4,1). The (4,1) cuts-on just below 1480 RPM. Figure 5.14 shows cancellation occurs in both radials over the RPM range tested. The transducers can minimize only the wall pressure, which in this case is the superposition of the (4,0) and (4,1) wall pressure. This is a function of spacing between all components of the system, since the phase speed varies with the cut-off ratio.

Figures 5.15 and 5.16 show a typical mode power map for the 28 vane control off and on cases. At this frequency the (4,0) is completely eliminated and (4,1) is reduced 9 dB. Spillover also occurs, limiting the total PWL reduction to 3.4 dB out of a possible 11.7 dB.

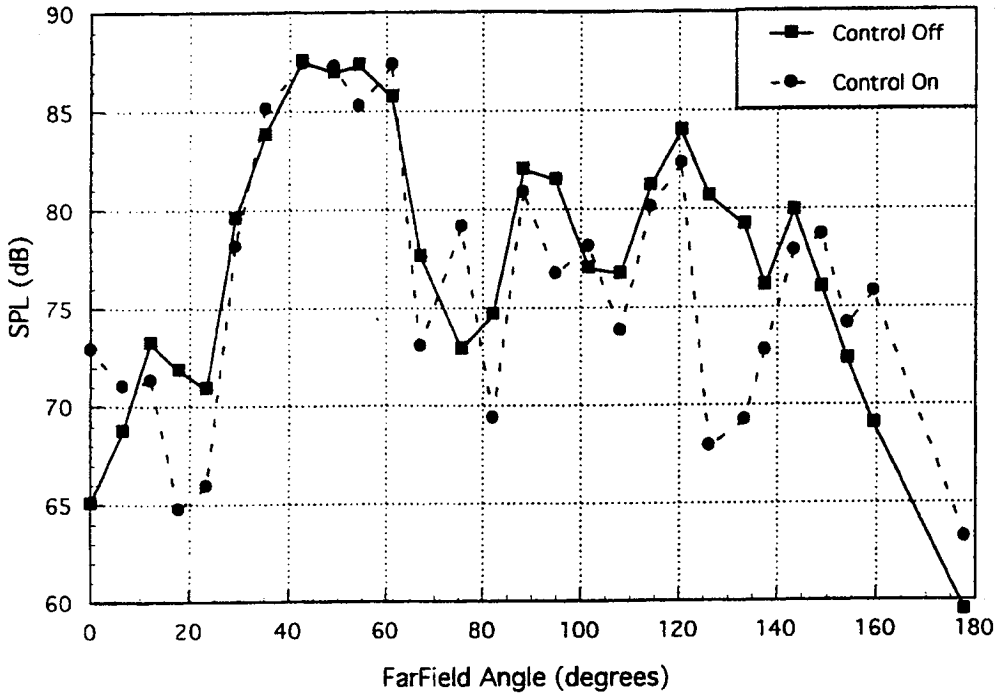

Figure 5.12 Farfield directivity plot. Ring aft, 2BPF, 1694 RPM, 920 Hz.

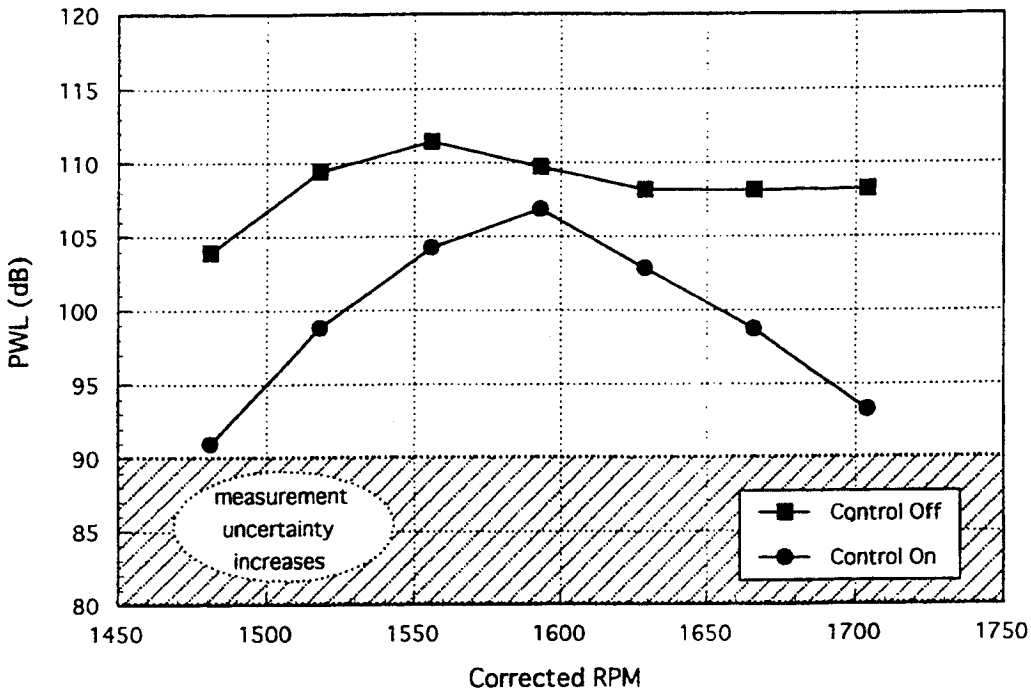

Figure 5.13 Mode m = 4 power levels in exhaust.

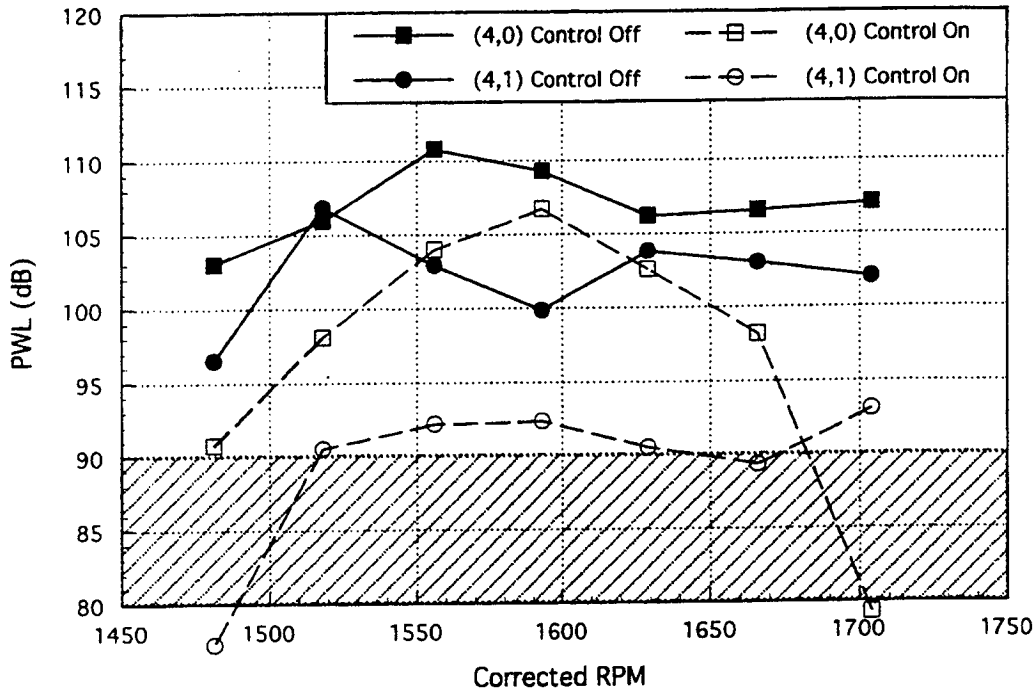

Figure 5.14 Mode (4,0) and (4,1) power levels in exhaust

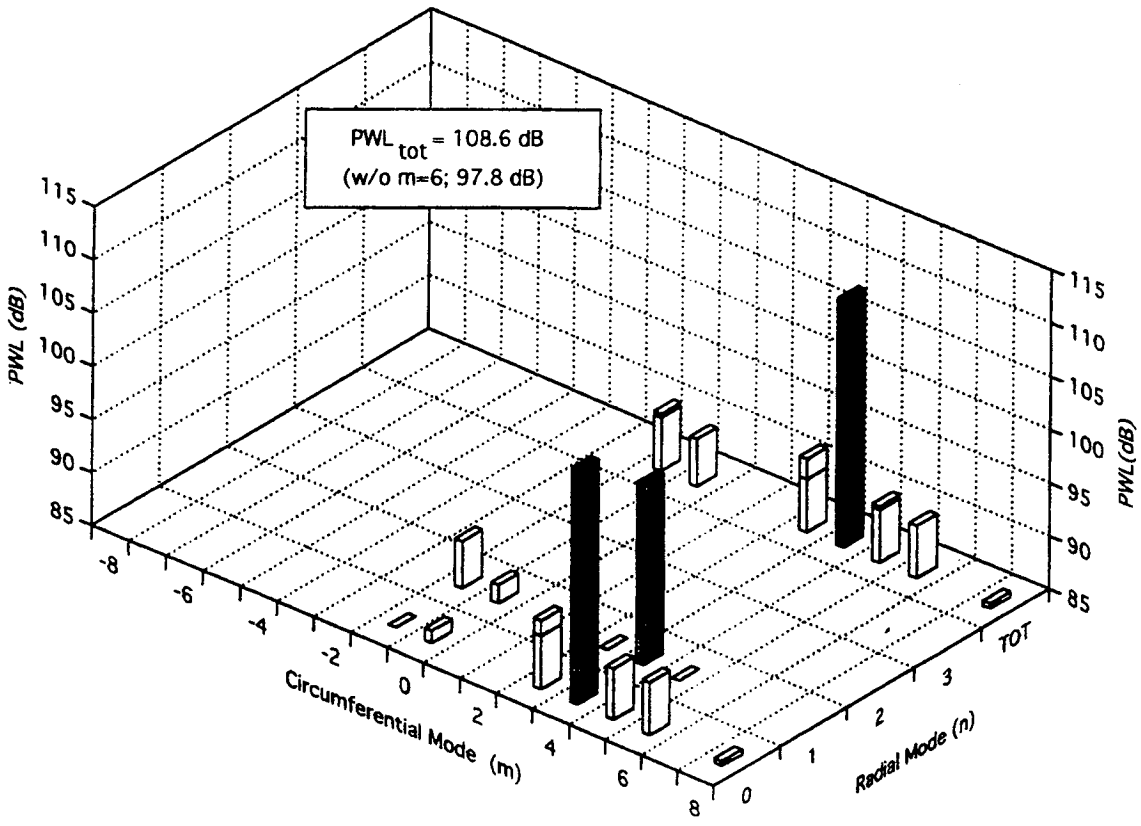

Figure 5.15 Control off mode power map. Aft, 2BPF, 1704 RPM, 920 Hz.

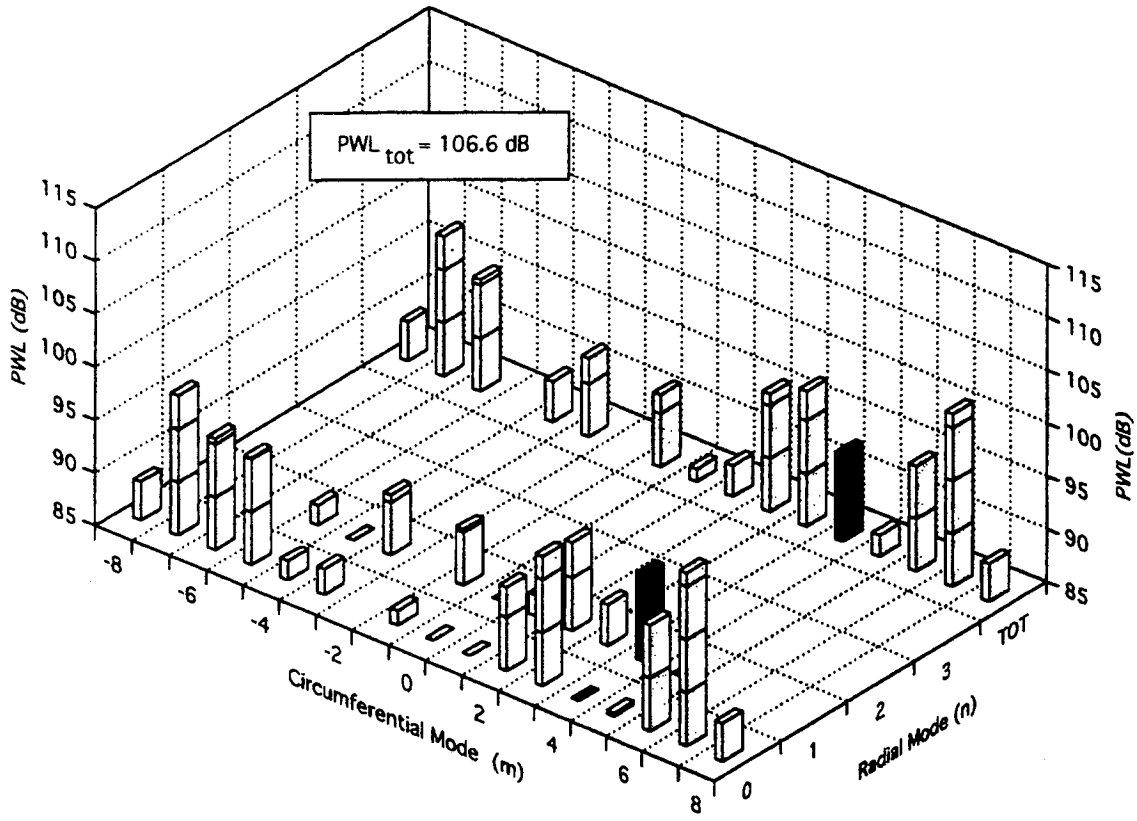

Figure 5.16 Control on mode power map. Aft, 2BPF, 1704 RPM, 920 Hz.

6. Conclusions and Recommendations

An active noise cancellation concept for a high-bypass turbofan was demonstrated. The system is based on a ring of flush mounted sources and a modal control approach. All sensors are contained within the fan duct.

The key results are that the (6,0) was completely eliminated at the 920 Hz design frequency and substantially reduced elsewhere. The total tone power was reduced 8.8 dB (out of a possible 11.6 dB). Farfield reductions of 13 dB (SPL) were obtained. The (4,0) and (4,1) modes were reduced simultaneously, yielding a 15 dB PWL decrease. The results indicate that global attenuation of PWL at the target frequency was obtained in the aft quadrant using an ANC actuator and sensor system totally contained within the duct.

The quality of the results depended on precise mode generation. High spillover into spurious modes generated by the ANC actuator array caused less than optimum levels of PWL reduction. The variation in spillover is believed to be due to the actuator calibration procedure, but must be confirmed in subsequent tests. Further investigation of the cause of spurious mode spillover is recommended, particularly as this might impact the accuracy requirements of the ANC actuator calibration and stability requirements of continuous operation.

Continuation of the development of an integrated analytical simulation that can be used to model the fan noise source and propagation, the coupling of the ANC actuators to the duct, the control system sensor signal pickup, and the control system algorithm data processing, is recommended. Incorporation of the effects of passive treatment into this simulation will further enhance its value as a design and evaluation tool in future studies.

In this study, ANC suppression was demonstrated for a single cut-on radial mode at the target spinning mode order. In order to develop ANC systems that will find eventual practical application in an aircraft engine fan duct, it will be necessary to tackle the problem of multiple cut-on radial modes in future efforts.

7. References

[1] Kraft R. E. and Kontos K. B., "Theoretical Implications of Active Noise Control for Turbofan Engines," AIAA paper 93-4355, Oct. 1993.

[2] Pla F. G. and Rajiyah H., "Active Control of Fan Noise - Feasibility Study. Volume 2: Canceling Noise Source Design of an Acoustic Plate Radiator Using Piezoceramic Actuators," NASA CR-195440, March 1995.

[3] Sutliff,, D. L., Nallasamy, M., Heidelberg, L. J., and Elliott, D. M., "Baseline Acoustic Levels of the NASA Active Noise Control Fan Rig", NASA TM-107214, also AIAA 96-1745, May, 1996.

[4] Cicon, D.E., Sofrin, T.G., and Mathews, D.C., "Investigation of Continuously Traversing Microphone System for Mode Measurement," NASA CR-16804, Nov. 1982.

[5] Tyler J.M., and Sofrin T.G., "Axial Flow Compressor Noise Studies," SAE Transactions, Vol. 70, 1962, pp. 309-332.

[6] Hall, D.G., Heidelberg, L., and Konno, K., "Acoustic Mode Measurements in the Inlet of a Model Turbofan using a Continuously Rotating Rake: Data Collection/Analysis Techniques," NASA TM 105963, Jan. 1993; also AIAA Paper 93-0599, Jan. 1993.

[7] Cooper, B.A., "A Large Hemi-Anechoic Chamber Enclosure for Community-Compatible Aeroacoustic Testing of Aircraft Propulsion Systems," Journal of the Institute of Noise Control Engineering of the USA, Jan/Feb 1994.

REPORT DOCUMENTATION PAGE

Form Approved
OMB No. 0704-0188

1. AGENCY USE ONLY (*Leave blank*)	2. REPORT DATE	3. REPORT TYPE AND DATES COVERED
	September 1996	Final Contractor Report

4. TITLE AND SUBTITLE

Active Control of Fan Noise: Feasibility Study
Volume 3: Active Fan Noise Cancellation in the NASA Lewis Active Noise Control Fan Facility

5. FUNDING NUMBERS

WU–538–03–11
C–NAS3–26617

6. AUTHOR(S)

Frederic G. Pla, Ziqiang Hu, and Daniel L. Sutliff

7. PERFORMING ORGANIZATION NAME(S) AND ADDRESS(ES)

General Electric Aircraft Engines
1 Neumann Way
P.O. Box 156301
Cincinnati, Ohio 45214–6301

8. PERFORMING ORGANIZATION REPORT NUMBER

E–10377

9. SPONSORING/MONITORING AGENCY NAME(S) AND ADDRESS(ES)

National Aeronautics and Space Administration
Lewis Research Center
Cleveland, Ohio 44135–3191

10. SPONSORING/MONITORING AGENCY REPORT NUMBER

NASA CR–198511

11. SUPPLEMENTARY NOTES

Frederic G. Pla and Ziqiang Hu, General Electric Aircraft, 1 Neumann Way, P.O. Box 156301, Cincinnati, Ohio 45214–6301 (work performed under NASA Contract NAS3–26617); Daniel L. Sutliff, National Research Council—NASA Research Associate at Lewis Research Center. Project Manager, Laurence J. Heidelberg, Propulsion Systems Division, NASA Lewis Research Center, organization code 2770, (216) 433–3859.

12a. DISTRIBUTION/AVAILABILITY STATEMENT

Unclassified - Unlimited
Subject Categories 07 and 71

This publication is available from the NASA Center for AeroSpace Information, (301) 621–0390.

12b. DISTRIBUTION CODE

13. ABSTRACT (*Maximum 200 words*)

This report describes the Active Noise Cancellation (ANC) System designed by General Electric and tested in the NASA Lewis Research Center's (LeRC) 48 inch Active Noise Control Fan (ANCF). The goal of this study is to assess the feasibility of using wall mounted secondary acoustic sources and sensors within the duct of a high bypass turbofan aircraft engine for global active noise cancellation of fan tones. The GE ANC system is based on a modal control approach. A known acoustic mode propagating in the fan duct is canceled using an array of flush-mounted compact sound sources. The canceling modal signal is generated by a modal controller. Inputs to the controller are signals from a shaft encoder and from a microphone array which senses the residual acoustic mode in the duct. The key results are that the (6,0) was completely eliminated at the 920 Hz design frequency and substantially reduced elsewhere. The total tone power was reduced 6.8 dB (out of a possible 9.8 dB). Farfield reductions of 15 dB (SPL) were obtained. The (4,0) and (4,1) modes were reduced simultaneously yielding a 15 dB PWL decrease. The results indicate that global attenuation of PWL at the target frequency was obtained in the aft quadrant using an ANC actuator and sensor system totally contained within the duct. The quality of the results depended on precise mode generation. High spillover into spurious modes generated by the ANC actuator array caused less than optimum levels of PWL reduction. The variation in spillover is believed to be due to calibration procedure, but must be confirmed in subsequent tests.

14. SUBJECT TERMS

Fan noise; Noise reduction; Ducted fans; Active control; Aircraft noise

15. NUMBER OF PAGES

51

16. PRICE CODE

A04

17. SECURITY CLASSIFICATION OF REPORT	18. SECURITY CLASSIFICATION OF THIS PAGE	19. SECURITY CLASSIFICATION OF ABSTRACT	20. LIMITATION OF ABSTRACT
Unclassified	Unclassified	Unclassified	